UNIVERSIDADE FEDERAL DE MINAS GERAIS
Escola de Engenharia
Programa de Pós-Graduação em Engenharia Metalúrgica, Materiais e de Minas

Tese de Doutorado

Comportamento de Amolecimento e Fusão de Cargas Ferrosas através de Abordagem Experimental e Modelo Termodinâmico

Autor: Ismael Vemdrame Flores
Orientador: Maurício Covcevich Bagatini
Co-orientador: Aline Lima da Silva

Novembro/2019

Ismael Vemdrame Flores

Comportamento de Amolecimento e Fusão de Cargas Ferrosas através de Abordagem Experimental e Modelo Termodinâmico

Tese apresentada ao Programa de Pós-graduação em Engenharia Metalúrgica, Materiais e de Minas da Escola de Engenharia da Universidade Federal de Minas Gerais, como requisito parcial para a obtenção do Grau de Doutor em Engenharia Metalúrgica, Materiais e de Minas

Área de concentração: Metalurgia Extrativa
Orientador: Maurício Covcevich Bagatini
Coorientador: Aline Lima da Silva

Belo Horizonte
Universidade Federal de Minas Gerais
Escola de Engenharia
2019

Flores, Ismael Vemdrame.
F634c Comportamento de amolecimento e fusão de cargas ferrosas através de abordagem experimental e modelo termodinâmico [recurso eletrônico] Ismael Vemdrame Flores. - 2019.
1 recurso online (xix, 84 f. : il., color.) : pdf.

Orientador: Maurício Covcevich Bagatini.
Coorientadora: Aline Lima da Silva.

Tese (doutorado) - Universidade Federal de Minas Gerais, Escola de Engenharia.

Apêndices: f. 77-84.

Inclui bibliografia.
Exigências do sistema: Adobe Acrobat Reader.

1. Engenharia metalúrgica - Teses. 2. Metalurgia extrativa - Teses. 3. Altos-fornos - Teses. 4. Microestrutura - Teses. 5. Porosidade - Teses. 6. Redução de minérios - Teses. I. Bagatini, Maurício Covcevich. II. Silva, Aline Lima da. III. Universidade Federal de Minas Gerais. Escola de Engenharia. IV. Título.

CDU: 669(043)

Ficha catalográfica: Biblioteca Profº Mário Werneck, Escola de Engenharia da UFMG

UNIVERSIDADE FEDERAL DE MINAS GERAIS
ESCOLA DE ENGENHARIA
Programa de Pós-Graduação em Engenharia Metalúrgica, Materiais e de Minas

PPGEM

Tese intitulada **"Comportamento de Amolecimento e Fusão de Cargas Ferrosas Através de Abordagem Experimental e Modelo Termodinâmico"**, área de concentração: Metalurgia Extrativa, apresentada pelo candidato **Ismael Vemdrame Flores**, para obtenção do grau de Doutor em Engenharia Metalúrgica, Materiais e de Minas, aprovada pela comissão examinadora constituída pelos seguintes membros:

Prof. Maurício Covcevich Bagatini
Orientador - Dr. (UFMG)

Profª Aline Lima da Silva
Coorientador - Drª (UFMG)

Prof. Roberto Parreiras Tavares
PhD (UFMG)

Prof. Leandro Rocha Lemos
Dr. (UFMG)

Prof. Cláudio Batista Vieira
Dr. (UFOP)

Guilherme Liziero Ruggio da Silva
Dr. (Gerdau Ouro Branco)

Prof. Rodrigo Lambert Oréfice
Coordenador do Programa de Pós-Graduação em Engenharia Metalúrgica, Materiais e de Minas/UFMG

Belo Horizonte, 05 de novembro de 2019

Dedico este trabalho ao meu pai, Sérgio Antônio Flores, pelo seu exemplo de pessoa e por todos os ensinamentos recebidos ao longo de minha vida.

AGRADECIMENTOS

Agradeço a todos aqueles que, direta ou indiretamente, colaboraram na preparação deste trabalho e, em particular:

À Deus, pois sem ele eu não teria chegado até aqui.

À minha querida esposa Thais pelo amor, companheirismo e apoio incondicionais e por acreditar em todo o meu potencial.

À minha família, em especial aos meus pais, Sérgio Antônio Flores e Rosa Maria Flores, e minha irmã, Rosiele Flores, pela compreensão, incentivo e carinho durante toda a minha trajetória acadêmica.

Ao professor Maurício Bagatini pela confiança em mim depositada, pela oportunidade de crescimento profissional e orientação acadêmica.

A professora Aline Lima da Silva pela sua coorientação e seus ensinamentos acerca do uso do software FactSage, sem os quais a criação do modelo termodinâmico não seria possível.

À Andreia Serrano pelo apoio e incentivo durante a redação dessa tese.

Aos alunos de iniciação científica do Laboratório de Processos Siderúrgicos da UFMG, Lucas Batista, Vitor Vianna, Rubia Teodoro, Otávio Matos, Arthur Lino, João Alves e Lucas Leal, pelo auxílio durante a realização da parte experimental desse trabalho.

Aos amigos Tiago Coser, Luiz Broilo, Bruno Flores, Vagner Machado, Nelson Freitas, Vinicius Ribeiro, Luan Assis, Thais Morato, Larissa Chaves, Lays Ribas, Thiago Suzuki, Fernanda Suzuki, Eduardo Silveira, Caique Matos e Rafael Lopes Jr. pela amizade e momentos de descontração.

Ao grupo Gerdau, em especial à Usina Ouro Branco, por financiar o reparo e o aperfeiçoamento do forno de amolecimento e fusão.

Ao amigo André Machado, pelos ensinamentos valiosos durante a etapa de reforma e aprimoramento do forno de amolecimento e fusão, os quais foram fundamentais para viabilizar este trabalho.

Ao professor Dagoberto Brandão Santos por, além de compartilhar seu conhecimento, disponibilizar toda estrutura necessária para o corte, preparação e visualização das amostras em microscopia óptica e eletrônica de varredura. Também agradeço ao seu aluno de iniciação Guilherme pelos ensinamentos quanto às etapas de preparação.

Ao coordenador do Programa de Pós-Graduação em Engenharia Metalúrgica, professor Rodrigo Lambert Oréfice, e sua equipe Maria Aparecida Pacheco e Nelson Antônio de Azevedo pela prontidão em resolver e aconselhar da melhor forma possível a resolução de qualquer problema.

À Coordenação de Aperfeiçoamento de Pessoal de Nível Superior pela concessão da bolsa de estudo.

SUMÁRIO

LISTA DE FIGURAS

LISTA DE TABELAS

LISTA DE NOTAÇÕES

$[\%CO]^{Inlet}$: concentração de CO em percentual em volumétrico no gás de entrada

$[\%CO]^{Outlet}$: concentração de CO em percentual em volumétrico no gás de saída

$[\%CO_2]^{Inlet}$: concentração de CO_2 em percentual em volumétrico no gás de entrada

$[\%CO_2]^{Outlet}$: concentração de CO_2 em percentual em volumétrico no gás de saída

$[\%N_2]^{Inlet}$: concentração de N_2 em percentual volumétrico no gás de entrada

$[\%N_2]^{Outlet}$: concentração de N_2 em percentual volumétrico no gás de saída

$\dot{m}_C$: taxa de deposição/consumo de carbono

$\dot{m}_{O,removed}$: taxa de remoção de oxigênio pela redução

M_C: massa molar de carbono

$m_{O,Removed}$: massa de oxigênio removida pela redução

$m_{O,Total}$: massa de oxigênio inicialmente presente nos óxidos de ferro

M_O: massa molar de oxigênio

V_0: volume padrão de um gás ideal a temperatura ambiente

W_1: massa da amostra medida no ar

W_2: massa da amostra completamente imersa em água

W_3: massa da amostra após sua imersão, com os poros ainda preenchidos com água

θ_{N_2}: vazão volumétrica de N_2 no gás de entrada

ρ_{H_2O}: densidade da água

$\rho_{apparent}$: densidade aparente

ρ_{true}: densidade real

O_r^T: oxigênio removido pela redução em uma dada temperatura

O_{total}: oxigênio inicial contido nos óxidos de ferro

RD_{exp}^T: grau de redução experimental em uma dada temperatura

RD_{sim}^{T}: grau de redução simulada em uma dada temperatura

B2: basicidade binária

B3: basicidade ternária

BEI: imagem de elétrons retroespalhados

C_2S: silicato dicálcico

E: resina epoxy

EDS: espectroscopia de energia dispersiva

F: faialita

I: ferro metálico

InRd: redução indireta

K: kelvin

kPa: kilo pascal

M: magnetita

MrRd: redução em estado líquido

NL/min: normal litro por minuto

P: poro

Pmax: perda de pressão máxima

PP: pontos percentuais

Q: quartzo

R.D.: grau de redução

R.R.: taxa de redução

R1: região de redução 1, redução gás/sólido

R_{1273}: grau de redução em 1273K

R_{1473}: grau de redução em 1473K

R2: região de redução 2, retardo de redução

R3: região de redução 3, redução em estado líquido

Raw: amostra em condição como recebida

RLM: microscopia de luz refletida

S Value: valor S, integral da curva de perda de pressão no intervalo de temperatura da zona coesiva

S&M: amolecimento e fusão

S: escória

SEM: microscopia eletrônica de varredura

Slag%T_{S2}: quantidade de escória na temperatura T_{S2}

$T_{10\%}$: temperatura de início de amolecimento

$T_{50\%}$: temperatura de final de amolecimento

$T_{50\%} - T_{10\%}$: intervalo de amolecimento

$T_{C10\%}$: temperatura onde a contração atinge 10%

T_D: temperatura de gotejamento

T_{E2}: temperatura de final de zona coesiva, onde a perda de pressão retorna a 2kPa

T_{ECZ}: temperatura de final de zona coesiva

T_{Pmax}: temperatura onde ocorre a máxima perda de preessão

$T_{pre\text{-}soft}$: temperatura de pré-amolecimento

T_{S2}: temperatura de início da zona coesiva, onde a perda de pressão ultrapassa 2 Kpa

$T_{SCZ} - T_{ECZ}$: intervalo de zona coesiva

T_{SCZ}: temperatura de início de zona coesiva

$T_{SlagFinal}$: temperatura onde da escória final

$T_{SlagForm}$: temperatura de formação do primeiro líquido

$T_{Slagmax}$: temperatura onde a quantidade de escória foi máxima

$T_{\Delta pm}$: temperatura de máxima perda de pressão

W: wüstita

Wt Pct: percentual em massa

XRD: difração de raios X

RESUMO

As propriedades de amolecimento e fusão das cargas ferrosas possuem papel fundamental na formação da zona coesiva. A posição e a espessura dessa região afetam fortemente a distribuição do fluxo gasoso e a eficiência da transferência de calor do alto-forno, os quais influenciam na permeabilidade e produtividade do reator. Durante a redução, amolecimento e a fusão das cargas ferrosas, importantes alterações de microestrutura ocorrem. O entendimento dessas mudanças em relação com os fenômenos de amolecimento e fusão é essencial para o desenvolvimento de novas matérias-primas, processos e modelos. Nesse contexto, o presente trabalho teve como objetivo investigar os fenômenos de amolecimento e fusão para três cargas ferrosas através de testes de amolecimento e fusão sob carga, e desenvolver um modelo termodinâmico capaz de abordar a evolução das fases ao longo dos diferentes estágios de redução, amolecimento e fusão. A parte experimental deste trabalho caracterizou as propriedades de amolecimento e fusão de um minério granulado, uma pelota ácida e um sínter através de testes de amolecimento e fusão convencionais. Além disso, testes interrompidos foram realizados, determinados em diferentes níveis de contração e perda de pressão, para obter amostras em diversos estágios do processo de amolecimento e fusão. Os produtos obtidos e as amostras como recebidas, foram caracterizadas por testes de densidade aparente e real (para calcular as porosidades aberta, fechada e total), difração de raios X, microscopia de luz refletida e microscopia eletrônica de varredura (com espectroscopia de energia dispersiva). Ademais, um modelo termodinâmico foi proposto utilizando o software FactSage e macroprocessamento. O modelo foi construído utilizando uma série de estágios de equilíbrio e operadores matemáticos (*splitters*) para realizar o controle do fluxo de matéria e para considerar a cinética de redução envolvida. A partir dos resultados experimentais, três regiões de redução principais foram caracterizadas: redução gás/sólido, retardo de redução e redução no estado líquido. Na primeira região de redução, a redução ocorreu de acordo com o modelo de núcleo não reagido, onde observou-se um aumento da porosidade aberta das amostras. Durante a região de retardo de redução, um acentuado decréscimo de porosidade aberta foi identificado, o que levou a uma diminuição significativa da taxa de redução indireta. Na região de redução no estado líquido, a escória (rica em FeO) inicialmente presente no núcleo das partículas exsudou

para o leito, levando a um acentuado aumento da taxa de redução devido ao contato da escória com os gases redutores e o coque. No início do amolecimento, as microestruturas dos materiais constituíram de wüstita pseudoglobular por pontos de escória. Com o andamento do aquecimento e da contração do leito, essa estrutura coalesceu, formando wüstita com formato globular em uma matriz de escória líquida. Em relação ao modelo termodinâmico, baseado em dados da literatura, a metodologia aplicada foi capaz de obter curvas de redução de acordo com os dados experimentais utilizados. Os operadores (*splitters*) usados para parcialmente considerar inibições cinéticas mostraram uma relação próxima a taxa de redução dos materiais. Além disso, os perfis calculados para a quantidade de líquido apresentaram uma boa relação com o comportamento experimental de amolecimento e fusão obtido da literatura. As temperaturas calculadas para a formação do primeiro líquido foram similares ao momento onde a contração de 10% dos leitos foi atingida, embora o nível de similaridade tenha dependido da heterogeneidade das amostras. Além disso, com o aumento da temperatura e consequentemente da quantidade de líquido, os resultados experimentais se aproximaram das condições de equilíbrio. Em especial, as frações de líquido calculadas foram similares aos perfis de perda de pressão experimentais, os quais qualitativamente determinam as características mais importantes da zona coesiva.

Palavras-chave: alto-forno, amolecimento e fusão, redução de minérios, microestrutura, porosidade, modelo termodinâmico.

ABSTRACT

The softening and melting properties of the iron-bearing materials play a decisive role in the formation of the cohesive zone. The position and thickness of this region greatly affect blast furnace gas flow distribution and heat-transfer efficiency, which influences furnace permeability and productivity. During the reduction, softening and melting of the iron-bearing materials, major microstructure changes occur. The understanding of such transformations and its relation with the softening and melting phenomena is essential to the development of new raw materials, technologies, and models. In this context, the present work sought to investigate the phenomena of the softening and melting process for three iron-bearing materials through softening and melting under load tests, and to develop a thermodynamic model to approach the phase evolution of the materials throughout its reduction, softening and melting. The experimental part of this work characterized the softening and melting properties of samples of lump ore, acid pellet, and sinter through conventional softening and melting under load experiments. Moreover, interrupted experiments were carried out, based on contraction and pressure drop levels, to obtain samples in specific moments of the softening and melting process. The products obtained and the samples as received were characterized by apparent and true density (used to calculate the open, closed and total porosity), X-ray diffraction, reflected light microscopy and scanning electron microscopy (with energy dispersed spectroscopy). Furthermore, a thermodynamic model was developed using FactSage thermodynamic software and macro-processing. The model was constructed using a series of equilibrium stages and mathematical operators (splitters) to determine flow directions of streams and to consider kinetic inhibitions. From the experimental results, three main regions of reduction were characterized, namely: solid/gas reduction, reduction retardation, and melting reduction. In the first reduction region, reduction occurred following the shrinking core model with the increasing of samples open porosity. On the reduction retardation region, a sharp decrease in open porosity was identified, which reflected on the diminishing of rate of indirect reduction. At the region of melting reduction, the slag (rich in FeO) initially present in the particles' core exuded to the bed, leading to a sharp increase in reduction rate due to slag contact with the reducing gas and coke. At the beginning of softening, the microstructure of the material was comprised of pseudo-

globular wüstite interspersed with slag. As heating progressed and bed contraction increased, that structure coalesced to form a globular shape wüstite in a well-connected liquid slag matrix. Regarding the thermodynamic model, based on literature data, the methodology applied was capable of obtaining iron-bearing materials reduction degrees in very good agreement to the experimental data used. The splitters used to partly consider kinetic inhibitions showed a close relation with the rate of reduction. Moreover, the calculated profiles of slag quantity showed a close relationship with the softening and melting behaviors evaluated from softening and melting experiments. The calculated first liquid formation temperature was similar to that of when the sample beds attained 10% contraction, although the level of similarity between those parameters depended on the level of heterogeneity of each raw material. In addition, as temperature and consequently the amount of liquid increased, samples appeared to get closer to equilibrium conditions. In especial, the liquid fractions were quite similar to the experimental profiles of pressure drop, which qualitatively determine the most important characteristics of the cohesive zone.

Keywords: blast furnace, softening and melting, ores reduction, microstructure, porosity, thermodynamic model.

Capítulo 1. Introdução, Objetivos e Estrutura da Tese

1.1. Introdução

O processo de redução de óxidos de ferro em alto-forno é a principal rota para produção de ferro primário da atualidade. Pelo topo desse reator, a carga ferrosa (minério granulado, sínter e pelota) e o coque metalúrgico (ou carvão vegetal) são carregados em camadas alternadas, enquanto ar pré-aquecido e combustíveis auxiliares são injetados pelas ventaneiras próximas à base do reator.

O aquecimento e a redução da carga ferrosa progridem à medida que essa desce, em contracorrente com os gases, pelo reator. Em um determinado nível de temperatura, a carga ferrosa passa pelo processo de amolecimento e fusão, dando origem a zona coesiva. Nessa região, a transição de sólido para líquido torna as camadas ferrosas impermeáveis à passagem do gás, o qual flui apenas através das camadas de coque. Por essa característica, a zona coesiva é responsável pela maior parcela da perda de pressão dentro do reator. A distribuição do fluxo gasoso (e térmico) através da carga sólida e consequentemente a produtividade do forno são fortemente influenciados pelo formato, posição e espessura da zona coesiva. Para maximizar a permeabilidade e produtividade do alto-forno, uma zona coesiva estreita é preferível, enquanto que o posicionamento mais baixo dessa zona no reator promove uma maior redução indireta da carga.

As características da zona coesiva podem ser controladas pelo perfil de distribuição da carga sólida e pelas propriedades de amolecimento e fusão (também chamadas de propriedades à quente) das matérias-primas ferrosas. No que se refere às matérias-primas, usualmente considera-se que o sínter metalúrgico possui melhores propriedades à quente do que pelotas e minérios, pois amolece em temperaturas mais elevadas e gera menores perdas de pressão. Comparativamente, cargas ácidas (minérios e pelotas) costumam apresentar características adversas, amolecendo em temperaturas relativamente baixas e produzindo maiores perdas de pressão. As características de amolecimento e fusão dependem do grau de redução, basicidade binária, quantidade de ganga e fluxantes, composição mineralógica e sua distribuição na microestrutura dos materiais.

No contexto de alto-forno, a redução das partículas acarreta em uma estrutura constituída por uma casca de ferro metálico que envolve um núcleo de fases na forma de óxidos. A formação de líquido nessa estrutura é responsável por desencadear a sequência de fenômenos associados ao amolecimento e fusão das cargas ferrosas. Esse líquido leva a uma diminuição da resistência à deformação das partículas, que contraem sob o peso da carga sólida acima da zona coesiva. Além disso, a porosidade da casca metálica tende a ser preenchida pelo líquido, prejudicando o andamento da redução indireta. À medida que a quantidade de líquido aumenta, a casca metálica rompe e a exsudação do líquido, anteriormente presente no núcleo das partículas, ocorre para o leito. O preenchimento dos espaços vazios do leito pelo líquido durante a exsudação diminui a permeabilidade da camada de carga ferrosa, levando a uma intensa elevação da perda de pressão. Além disso, nesse momento há o rápido crescimento da taxa de redução devido ao contato da escória (rica em FeO) com os gases redutores e o coque metalúrgico.

Para verificar as propriedades à alta temperatura das cargas ferrosas, usualmente empregam-se experimentos de amolecimento e fusão sob carga. Nesses testes, um leito da carga ferrosa é submetido à aquecimento contínuo sob atmosfera redutora e aplicação de carga mecânica, enquanto medem-se a deformação e perda de pressão através do leito. Até o momento, nenhum órgão de padronização definiu em norma parâmetros para a execução e interpretação de testes de amolecimento e fusão. Isso torna a comparação de resultados entre laboratórios uma tarefa árdua devido à grande diversidade de equipamentos. No Brasil, somente três equipamentos do tipo podem ser encontrados. Um no Centro de Tecnologia de Ferrosos da Vale, outro no Centro de Pesquisa da Usiminas Ipatinga e, mais recentemente, o equipamento desenvolvido no Laboratório de Processos Siderúrgicos da UFMG.

Para investigar os fenômenos de amolecimento e fusão, testes interrompidos em temperaturas (ou níveis de deformação/perda de pressão) de interesse são utilizados para gerar amostras que representam os diferentes estágios de amolecimento e fusão. Para tanto, duas abordagens são encontradas na literatura. A primeira realiza a pré-redução da carga ferrosa até o nível desejado em um primeiro equipamento, e posteriormente, submete o material resultante a um experimento de amolecimento e fusão (segundo

equipamento), utilizando nitrogênio até a interrupção. A segunda abordagem realiza o aquecimento e redução da amostra de forma contínua e com aplicação de carga mecânica até que o ponto de interesse para interrupção seja atingido. Essa última se aproxima melhor das condições reais observadas durante a descida da carga nos altos-fornos. No entanto, a maior parte dos estudos fundamentais voltados para determinar os fenômenos de amolecimento e fusão e a evolução da microestrutura de diferentes cargas ferrosas foi realizado utilizando a abordagem com pré-redução. Assim, investigações de base utilizando a segunda abordagem para os testes interrompidos e posterior caracterização da microestrutura e fenômenos envolvidos ainda é necessitada pela literatura.

Devido ao caráter multifásico e multicomponente do amolecimento e fusão, o uso da termodinâmica, como diagramas de fase e cálculos de equilíbrio, é regularmente empregado para elucidar o comportamento de cargas ferrosas em alta temperatura. No entanto, a literatura atual carece de modelos termodinâmicos voltados para investigar os fenômenos de redução, amolecimento e fusão. Duas das prováveis razões para isso são as barreiras cinéticas envolvidas e a heterogeneidade das cargas ferrosas, as quais podem produzir grande variabilidade entre os modelos e a realidade. Uma possível alternativa para contornar os desvios cinéticos é combinar a robustez dos cálculos termodinâmicos realizados por softwares computacionais com o controle do fluxo de matéria (ou do andamento das reações) através de operadores matemáticos baseados em dados experimentais.

Nas últimas décadas houve um decréscimo considerável da qualidade das matérias-primas ferrosas, levando a obtenção de cargas ferrosas de menor qualidade. Nesse cenário, uma abordagem experimental consistente para determinação das propriedades à quente das cargas ferrosas e a elucidação dos fenômenos envolvidos é fundamental. Além disso, a capacidade de modelar as alterações de composição química e mineralógica continuamente em função da temperatura pode trazer uma nova visão quanto aos mecanismos de amolecimento e fusão. A contribuição teórica e flexibilidade desses modelos, associados com o conhecimento fenomenológico existente pode promover a obtenção de ferramentas de previsão e controle em diversos cenários.

1.2. Objetivos

1.2.1. Objetivos Geral

O propósito da presente tese foi investigar os fenômenos e mecanismos envolvidos no processo de amolecimento e fusão de três cargas ferrosas utilizadas em alto-forno através de testes de amolecimento e fusão interrompidos e também desenvolver um modelo termodinâmico computacional incorporando limitações cinéticas para abordar de forma contínua a redução dos óxidos de ferro, bem como a evolução das fases sólidas e líquidas relacionadas ao processo amolecimento e fusão, para servir como ferramenta de modelagem.

1.2.2. Objetivos Específicos

Como objetivos específicos desse estudo, destacam-se:

- Determinar as propriedades à quente de um minério granulado, uma pelota ácida e um sínter através de experimentos de amolecimento e fusão sob carga utilizando a metodologia desenvolvida na UFMG;
- Realizar os experimentos interrompidos para a obtenção de amostras de interesse dentro do intervalo de amolecimento e fusão, bem como caracterizar a evolução das fases e da microestrutura dos produtos obtidos;
- Desenvolver um modelo termodinâmico computacional capaz de simular o grau e a taxa redução de cargas ferrosas em testes de amolecimento e fusão, utilizando restrições cinéticas;
- A partir do modelo, calcular a evolução da composição de fases de diferentes matérias-primas ferrosas em função da temperatura. Além disso, comparar esses resultados com os fenômenos de amolecimento existente na literatura e com os parâmetros usualmente empregados na avaliação do comportamento em alta temperatura de cargas ferrosas.

1.3. Estrutura da Tese

A presente proposta de tese foi dividida em 7 capítulos, sendo que o presente capítulo se refere a introdução, objetivos e estrutura do estudo e os Capítulos 2 e 3 correspondem, respectivamente, a um manuscrito publicado e outro submetido para publicação em periódico internacional.

No Capítulo 2 é apresentado o manuscrito submetido ao periódico Metallurgical and Materials Transactions B (Qualis A1), onde foi avaliado o comportamento de redução, amolecimento e fusão de três cargas ferrosas distintas. Nesse trabalho foram realizados testes interrompidos com o intuito de elucidar os fenômenos envolvidos nos diferentes estágios de amolecimento e fusão de três tipos de cargas ferrosas distintas. Para isso, utilizou-se de testes de densidade, difração de raios X, microscopia óptica e microscopia eletrônica de varredura, que permitiram identificar a evolução da densidade (real e aparente), porosidade (aberta, fechada e total), composição das fases e microestrutura ao longo do processo de amolecimento e fusão.

O Capítulo 3 corresponde ao manuscrito publicado no periódico internacional Metallurgical and Materials Transactions B (Qualis A1) em agosto de 2019. Nesse estudo foi desenvolvido um modelo termodinâmico a partir do software FactSage, combinado com etapas de macroprocessamento para considerar as limitações cinéticas (através de operadores chamados *splitters*) envolvidas na redução das cargas ferrosas. Após modeladas as curvas de redução, a evolução das fases condensadas e líquidas foi avaliada em função da temperatura e os resultados obtidos foram comparados com os parâmetros de contração e perda de pressão oriundos de testes de amolecimento e fusão.

O Capítulo 4 se refere às considerações finais realizadas a partir dos resultados apresentados nos capítulos 2 e 3. Nesse capítulo, os resultados mais importantes obtidos foram brevemente discutidos e relacionados, mostrando a importância de ambas as abordagens realizadas para compreender os fenômenos de amolecimento e fusão.

Por fim, o Capítulo 5 apresenta as contribuições originais para o conhecimento, enquanto que o Capítulo 6 lista as publicações realizadas ao longo do período em que esse estudo foi realizado. O Capítulo 7 exibe as sugestões de trabalhos futuros que visam dar continuidade aos tópicos levantados ao longo desse trabalho.

Os apêndices A, B e C apresentam maiores detalhes sobre as técnicas para determinação de densidade aparente e real, o aspecto visual dos leitos de amostra interrompidos e uma explicação mais detalhada sobre a concepção do modelo termodinâmico.

Capítulo 2. Artigo A. Microstructure and Porosity Evolution During the Reduction, Softening and Melting of Iron-bearing Materials

Ismael Vemdrame Flores[a*], Otávio Matos[a], Aline Lima da Silva[b], Maurício Covcevich Bagatini[a]

[a]Ironmaking Processes Laboratory (LPS), Federal University of Minas Gerais (UFMG), PO Box 31270-901, Belo Horizonte, Brazil.

[b]Metallurgical and Materials Department, Federal University of Minas Gerais (UFMG), PO Box 31270-901, Belo Horizonte, Brazil.

*Corresponding Author

Abstract

The performance of the blast furnace is strongly affected by the position and thickness of the cohesive zone, which is largely influenced by the high-temperature properties of the iron-bearing materials. During its reduction, softening and melting, ferrous materials undergo major microstructure changes and its understanding is essential to develop new raw-materials, technologies, and models. In this study, the behavior of reduction, softening and melting of a lump ore, an acid pellet, and a sinter was characterized by softening and melting (S&M) experiments. After that, to access the samples' structural transformations, interrupted S&M tests were carried out up to four different conditions based on contraction and pressure drop levels. The obtained products were characterized according to its density (true and apparent), porosity (open, closed and total), phase composition by X-ray diffraction and microstructure (reflected light microscopy and electron scanning microscopy). From the S&M test results, three main regions of reduction were characterized, namely: solid/gas reduction, reduction retardation, and melting reduction. In the solid/gas reduction, samples open porosity increased, with reduction following the shrinking core model. On the region of reduction retardation, a sharp decrease in open porosity was identified together with the diminishing of the

reduction rate, which occurred due to the iron shell porosity being clogged due to the slag transfer from the particles' cores to its periphery. At the melting exudation region, reduction retardation ceased and exudation of the ferrous slag lead to a peak of reduction. The lower the reduction degree of the samples at this stage, the higher the consumption of carbon. Furthermore, at 10% contraction, a pseudo-globular wüstite structure interspersed with slag was observed for the pellet and sinter cores. At 50% contraction, the previous structure coalesced to form a globular shape wüstite in a well-connected slag matrix.

Keywords: softening and melting, iron-bearing materials, blast furnace, microstructure, reduction retardation, porosity

2.1. Introduction

The phenomenon of softening and melting of iron-bearing materials occurs during the descent of the burden through the blast furnace, originating the region known as the cohesive zone. The performance of the blast furnace is strongly affected by the position and thickness of this region, which is largely influenced by the high-temperature properties of the iron-bearing materials[1-3]. The process of reduction, softening and melting involves major changes in the microstructure of the iron-bearing materials, which understanding is essential to the development of new raw materials, technologies, and models.

According to Bakker et al.[4], the formation of a liquid slag inside the agglomerates during the heating and reduction of iron oxides is crucial to trigger softening and melting. Through softening, it is understood that a bed of particles and the particles itself start to deform under a compressive force. However, the formation of the first liquid will depend on the materials' chemical composition, morphology and type (lump, pellet or sinter)[5]. As the process advances the liquid fraction existent at particles increases[2] and at some point, the retardation of the rate of reduction occurs. That phenomenon is caused as the melt formed in the core of particles exudes into the shell, inducing sintering of the metallic iron under the presence of a liquid phase[6]. The limitation of reduction also influences

the extent of melting reduction, implying that there is danger of blast furnace chilling[6]. Moreover, the works of Clixby et al.[7] and Ritz et al.[8] demonstrate the importance of iron-bearing materials having good reducibility, where the greater the reduction degree the higher the softening and melting temperatures.

To understand the microstructure evolution of iron-bearing materials, usually interrupted softening and melting under load tests are applied to obtain samples that represent a given high-temperature condition[9]. For that, two main approaches can be used, one pre-stablishes the level of reduction degree of a given material and then carry out a softening and melting test under nitrogen. The second approach realizes the reduction continuously with heating while a mechanical load is applied, at the same time recording the softening and melting results. The latter better approximate to the real phenomena occurring in the blast furnace, but increase the complexity of the results and its interpretation. However, most of the base and fundamental studies for softening and melting of iron-bearing materials were carried out utilizing the pre-reduction approach[1,6,10-12]. With that methodology, different ferrous materials are usually pre-reduced to the same reduction degree, which can in part eliminate softening and melting differences intrinsically related to reduction as the wüstite content significantly influences the formation and properties of primary melt[13,14].

Moreover, several papers have been applying thermodynamic to better understand the softening and melting phenomena[10, 12, 15-19]. In a recent paper [20], the authors presented the current state of an on-development thermodynamic model using FactSage and macro processing operations to simulate the material phase evolution through the entire temperature interval of reduction, softening and melting. The model was mostly constructed over literature data[18]. However, studies containing all the necessary information to further developed the model and validate it are quite scarce.

In this context, the present research aimed to characterize the phenomena of reduction, softening and melting occurring for three different iron-bearing materials also accessing its microstructure and porosity evolution. For that, samples were obtained through the interruption of continuous softening and melting experiments. In addition, the data

obtained will provide valuable support to the further development of the said thermodynamic model.

2.2. Experimental

2.2.1. Raw Materials

To access the high-temperature properties of different ferrous materials, a lump ore, an acid pellet, and a sinter were selected. All samples obtained were in current use by an ironmaking company at Minas Gerais, Brazil. The chemical composition of all iron-bearing raw materials is presented in Table 2.1. The appearing of the samples is shown in Figure 2.1.

Table 2.1. Raw materials chemical composition

	Chemical Composition (Wt Pct)							B2[a]	B3[b]	LOI[c]	Gangue (Wt Pct)
	Fe_t	FeO	CaO	SiO_2	Al_2O_3	MgO	P				
Lump	65.15	-	0.88	1.95	1.31	0.33	0.048	0.45	0.62	1.92	4.5
Pellet	63.25	-	1.81	5.13	1.11	0.68	0.047	0.35	0.49	-	7.7
Sinter	57.60	6.05	8.66	5.66	1.48	1.48	0.046	1.53	1.79	-	17.3

[a]Binary Basicity ($B2 = CaO/SiO_2$); [b]Ternary Basicity ($B3 = (CaO+MgO)/SiO_2$); [c]Loss on ignition

2.2.2. Softening and Melting Experiments

The softening and melting characteristics of the samples were evaluated using the apparatus shown in Figure 2.1. For the tests, a packed bed comprised of the ferrous material (40 mm height) packed in-between two coke layers (20 mm each) was heated up to 1773 K in a graphite crucible (48 mm internal diameter). Subject to the condition of constant layer thickness, samples weighted differently depending on its bulk density. All materials were used with particle size between 10 and 12.5 mm and were dried at 105°C for 24 hours before testing.

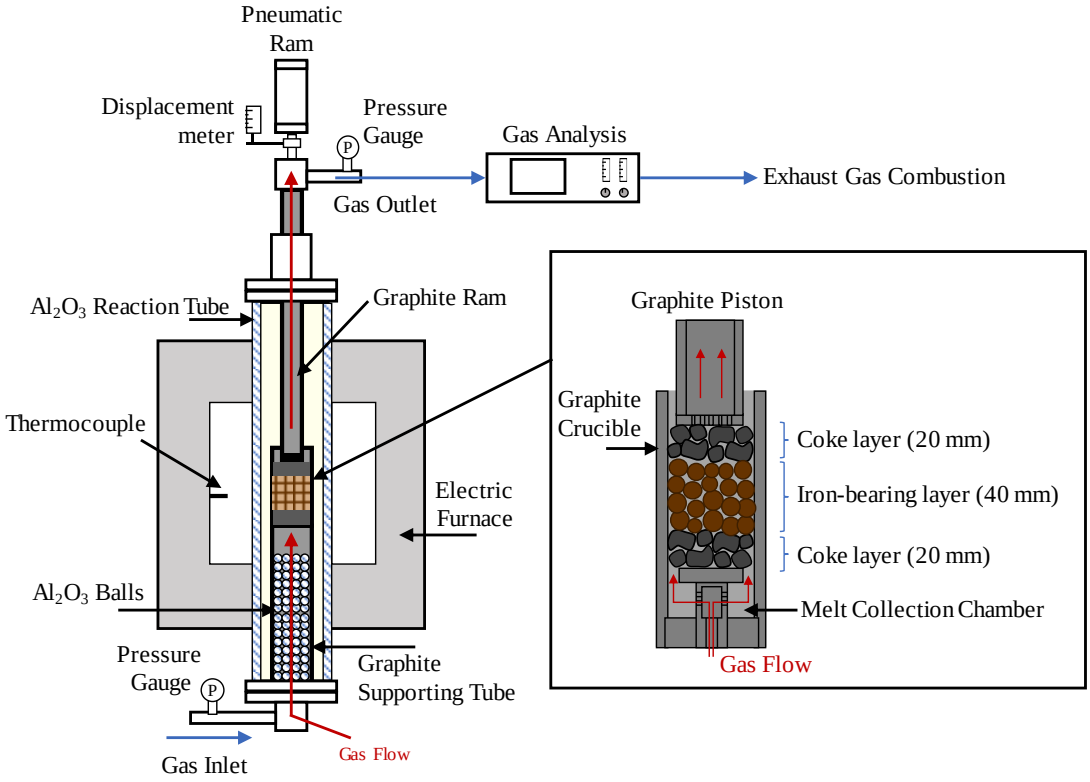

Figure 2.1. Schematic diagram of the experimental apparatus used for the softening and melting tests.

The experimental conditions utilized in the experiments can be seen in Figure 2.2. The furnace was heated from room temperature up to 1273 K at a heating rate of 10 K/min, which afterward was changed to 5 K/min up to 1773 K. A pure nitrogen atmosphere was kept until the temperature of 1073 K was reached, at this point a mechanical load of 100kPa was applied over the sample bed using a pneumatic ram and the nitrogen stream was switched for a reducing gas mixture of 30% CO and 70% N_2 (total flow rate of 8 NL/min) using mass flow controllers. After reaching its maximum temperature (1773 K) the sample was cooled under a nitrogen flow rate of 5.6 NL/min. The difference between the furnace and crucible thermal profiles is also shown in Figure 2.2. In the course of each test, samples displacement and pressure drop, as well as the outlet gas composition, were recorded using a data acquisition system. A minimum of two repetitions was carried out for each material and the results presented are expressed as the average values.

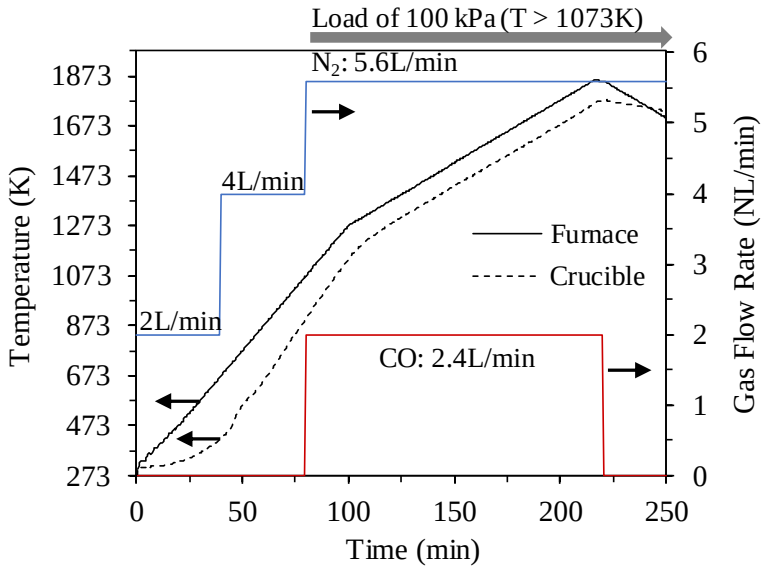

Figure 2.2. Experimental conditions used in the softening and melting tests.

To evaluate each iron-bearing material behavior, the contraction of the samples was calculated from the displacement measurements, while the pressure drop across the bed directly measures the changes in bed permeability due to the softening and melting phenomena. Moreover, the reduction behavior of the samples was evaluated by the progress of its reduction degree, calculated by Equation 2.1, where $m_{O,Removed}$ is the mass of oxygen removed from the sample at a given temperature and $m_{O,Total}$ is the mass of oxygen initially present in the iron oxides. The value of $m_{O,Removed}$ was obtained by the continuous outlet gas analysis regarding CO, CO_2, and N_2 by applying the mass balances of oxygen and carbon expressed in Equations 2.2 and 2.3[21], respectively. Equation 2.2 gives the rate of oxygen removal ($\dot{m}_{O,removed}$) from the difference in oxygen content between the inlet (directly from the mass flow controllers) and outlet gases (gas analysis). Equation 2.3 determines the rate of carbon consumption or deposition in the test, represented by positive and negative values respectively. In those equations, [%i] represents the volume percentage of the gaseous species "i" for inlet and outlet gases, θ_{N_2} is the volume flow rate of N_2 introduced in the experiments by the mass flow controllers, M_O e M_C are the molar masses of oxygen and carbon, and V_0 is the standard volume of an ideal gas at room temperature. The value of $m_{O,Removed}$ is obtained by integrating the rate of oxygen removal (Equation 2.2) overtime after all calculations are corrected for carbon deposition (at low temperature, below 1023-1073K[21]) and carbon gasification (Boudouard reaction, at higher temperatures) from Equation 2.2. The parameters used to

evaluate the softening and melting phenomena and compare the different samples are summarized in Table 2.2.

$$\text{Reduction Degree (\%)} = {}^{m_{O,Removed}}/_{m_{O,Total}} \text{ x } 100 \quad [2.1]$$

$$\dot{m}_{O,removed} = \left(\frac{[\%CO]^{Outlet}+2x[\%CO_2]^{Outlet}}{[\%N_2]^{Outlet}} - \frac{[\%CO]^{Inlet}+2x[\%CO_2]^{Inlet}}{[\%N_2]^{Inlet}}\right) x \frac{\theta_{N_2} x M_O}{V_0} \quad [2.2]$$

$$\dot{m}_C = \left(\frac{[\%CO]^{Inlet}+[\%CO_2]^{Inlet}}{[\%N_2]^{Inlet}} - \frac{[\%CO]^{Outlet}+[\%CO_2]^{Outlet}}{[\%N_2]^{Outlet}}\right) x \frac{\theta_{N_2} x M_C}{V_0} \quad [2.3]$$

Table 2.2. Parameters used to characterize softening and melting.

Symbols	Meaning	Units
$T_{10\%}$	The start of softening temperature; 10% contraction	K
$T_{50\%}$	The end of softening temperature; 50% contraction	K
T_{SCZ}	The cohesive zone starting temperature; reaches 1 kPa pressure	K
$T_{\Delta pm}$	The temperature at which the pressure drop is maximum	K
T_{ECZ}	The cohesive zone ending temperature; return to 1 kPa pressure	K
$T_{50\%} - T_{10\%}$	The softening temperature interval	K
$T_{SCZ} - T_{ECZ}$	The cohesive zone temperature interval	K
Pmax	The maximum value of pressure drop	kPa
R_{1273}	Reduction degree at 1273K	%
R_{1473}	Reduction degree at 1473K	%
RR_{1273}	Reduction rate at 1273K	%/min
RR_{1473}	Reduction rate at 1473K	%/min
S Value = ΔP x ΔT	The integral of pressure drop with temperature in the cohesive zone interval	kPa x K

Besides the standard complete softening and melting tests, a large number of experiments were interrupted at reaching specific temperatures of interest. This was done by using the same experimental conditions mentioned up to the desired temperature, at which the heating program was changed to cooling at a constant rate, the mechanical load was removed, and the reducing gas was substituted by a stream of pure nitrogen at 5.6 NL/min. The objective of such tests was to produce "snap-shots" of the ferrous materials at different stages of softening and melting. The interrupted products were characterized according to the flow diagram in Figure 2.3 and each analysis is described below.

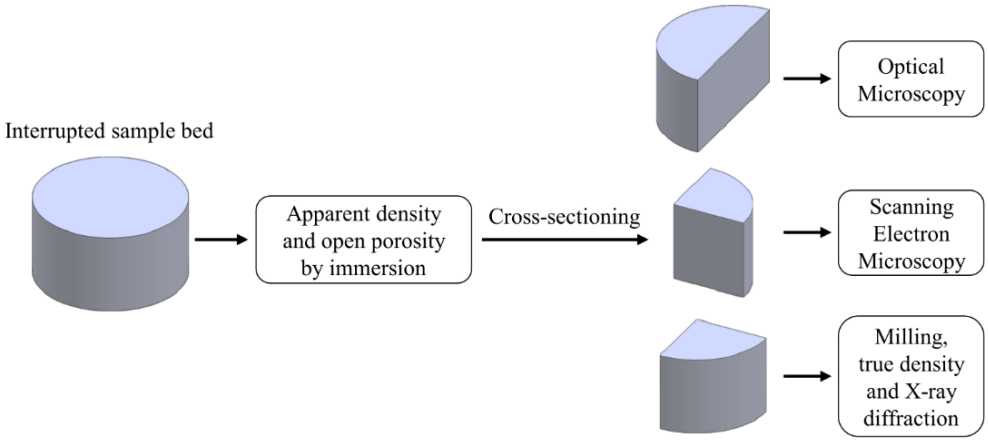

Figure 2.3. Flow chart of the procedures used to characterize the samples from interrupted tests.

2.2.2.1. X-ray Diffraction

All ferrous iron-bearing materials and the samples from the interrupted tests (particle size under 0.044 mm) were submitted to X-ray diffraction (XRD) to determine the evolution of the sample phases composition. For that, a Philips-PANalytical PW1710 diffractometer was employed, using Cu Kα source, scanning goniometry interval of 1 second for 0.06° of a degree from 3 to 90°, respectively.

2.2.2.2. Density and Porosity

Raw and interrupted samples' apparent density was determined using the immersion method[22]. From the Archimedes' principle, the buoyant force on a submerged object is equal to the weight of the fluid that is displaced by the object, allowing an easy determination of samples' volume. The method determines: W_1 – the weight of sample (dried) measure in air; W_2 – the weight of sample fully immersed in water; and W_3 – the weight of sample with its open pores soaked with water after immersion (W_3), which can be used in Equations 2.4 and 2.5 to calculate the materials apparent density and open porosity. All immersion tests were repeated five times.

$$\rho_{apparent}\ (g/cm^3) = \rho_{H_2O}\ x\ \left(W_1 \Big/ W_3\text{-}W_2\right) \qquad [2.4]$$

$$\text{Open porosity (\%)} = 100 \times {(W_3 - W_1)}/{(W_3 - W_2)} \quad [2.5]$$

The true density (ρ_{true}) of the samples was determined by water pycnometry according to the ASTM D167 standard. Those measurements were carried out in triplicates. From the results of true and apparent density, the total porosity of the materials was calculated by Equation 2.6. The closed porosity was obtained by the difference between total and open porosities.

$$\text{Total porosity (\%)} = 100 \times (1 - {\rho_{apparent}}/{\rho_{true}}) \quad [2.6]$$

2.2.2.3. Microstructure Investigation

The samples from the interrupted tests were cut along the direction of mechanical load application, mounted in resin and prepared to observation using reflected light microscopy (RLM) and scanning electron microscopy (SEM). In addition to the SEM, electron (EDS) and chemical maps were carried out.

2.3. Results and Discussion

2.3.1. Softening and Melting Experiments Results

Figure 2.4 presents the variations of reduction degree (R.D.), contraction and pressure drop from the softening and melting experiment carried out for the lump ore, acid pellet, and sinter. Also, Figure 2.4-a illustrates some of the parameters (Table 2.2) used to characterize the materials softening and melting.

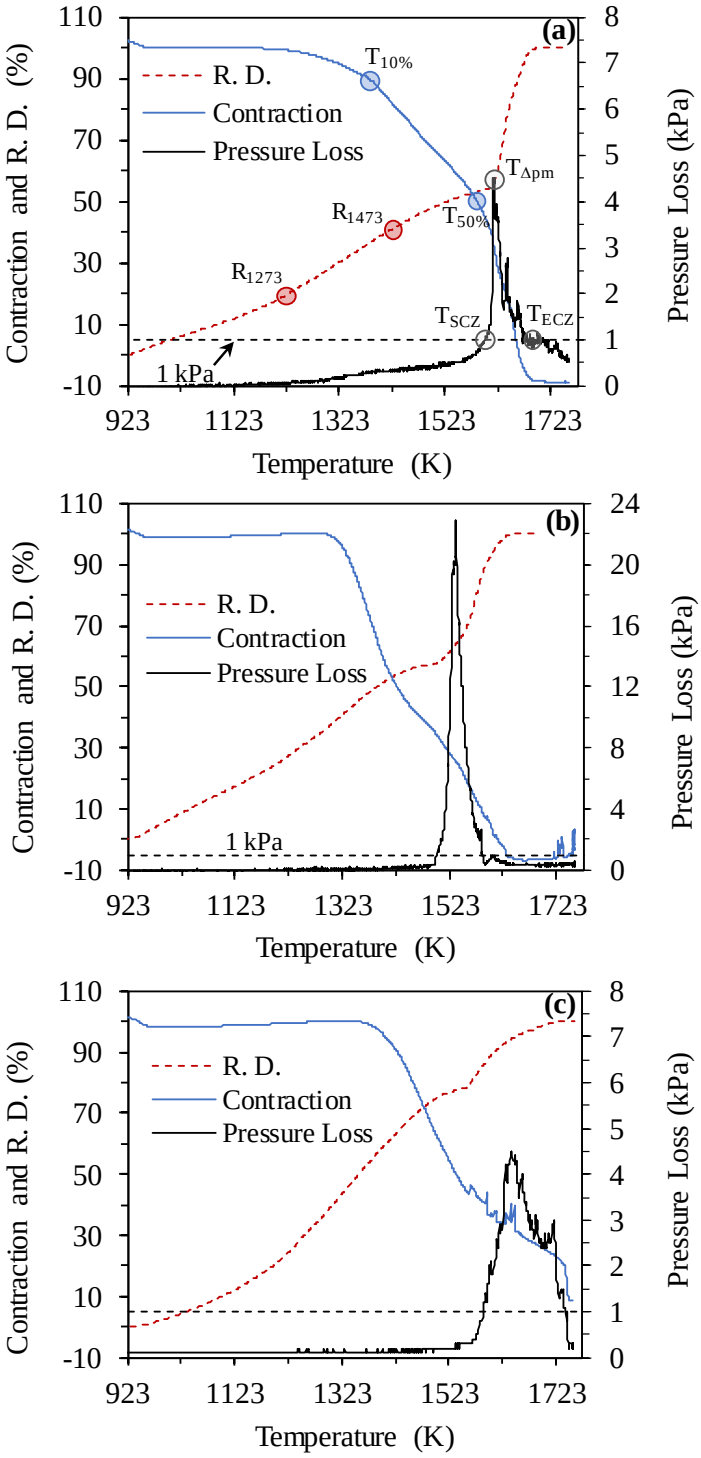

Figure 2.4. Softening and melting results for the (a) lump ore, (b) acid pellet and (c) sinter. The horizontal dashed line indicates the limit of pressure loss (1kPa) used to determine cohesive zone temperatures.

All samples presented the same general behavior of softening and melting, which according to Bakker et al.[4] can be divided into four main stages (pre-softening, softening,

melt exudation and melting down) based on the variations of bed contraction and pressure drop. At the pre-softening stage samples' contraction and pressure drop are practically stable, while the R.D. constantly increases with temperature. Depending on the material type, different rates of reduction (slopes of the reduction degree curves) were observed. The second stage of the softening and melting sequence, i.e. softening stage, is identified by the gradual contraction of the bed while no significant change in pressure drop occurs. The contraction rate at this stage is relatively constant for each sample until the next stage is reached. The transition from the softening to the melt exudation stage is identified by the abrupt and sharp increase in the pressure drop across the bed, resultant from the exudation of ferrous melt, initially present within the particle's cores, into the bed voidage. At the exudation stage, a change in the contraction rate was observed for all samples. The final stage of softening and melting is the melting down stage, characterized by the actual dripping of melt (iron and/or slag) from the whole bed.

The high-temperature characteristics of the samples studied are summarized by the parameters shown in Table 2.3. Overall, small standard deviations were obtained between repetitions, showing the test had good repeatability. From the reduction indexes (R_{1273} and R_{1473}), the sinter showed better reducibility achieving an R.D. of 74 % at 1473 K. In comparison, at that same temperature, the lump ore reduced only up to 47 %, while the pellet reducibility was intermediate (57 %). It is interesting to see that at 1273 K, the pellet and the sinter achieved the same R.D. (34 %), however, the pellets showed a quite significant decrease of reduction rate (R.R.) at approximately 1423K due to the phenomena of reduction retardation (Figure 2.4-b). The latter can be also seen at Table 2.3 by the low value of RR_{1473} of the acid pellet (0.13%/min) in comparison to the lump ore (0.44 %/min) and the sinter (0.70 %/min). Regarding the reduction rates at the temperature of 1273K (RR_{1273}), the sinter showed the higher reduction velocity, followed by the pellet and the lump ore. Moreover, from 1273 to 1473 K, R.R. sharply decreased for the acid pellet. Such effect was less pronounced for the lump ore and was moderate for the sinter. Overall, higher R.R. were observed for the sinter.

Table 2.3. Parameters from the softening and melting experiments.

		Lump Ore		Acid Pellet		Sinter	
Parameter	Unit	Average	S.D.[a]	Average	S.D.	Average	S.D.
Charge	g	165.7	6.6	133.4	2.8	123.7	1.3
$T_{10\%}$		1376	8.3	1340	0.5	1423	2.8
$T_{50\%}$		1582	8.1	1423	1.5	1528	5.7
T_{SCZ}		1598	5.5	1502	2.5	1577	10.3
$T_{\Delta pm}$	K	1617	2.6	1541	6.4	1626	12.8
T_{ECZ}		1661	9.4	1590	3.9	1737	6.4
$T_{50\%} - T_{10\%}$		206	16.0	83	2.0	105	2.8
$T_{SCZ} - T_{ECZ}$		62	3.9	88	1.5	164	5.3
Pmax	kPa	4.3	0.3	22	0.9	4.4	0.4
R_{1273}	%	25	2.1	34	0.1	34	0.1
R_{1473}	%	47	4.3	57	0.2	74	1.7
RR_{1273}	%/min	0.58	0.02	0.70	0.006	1.05	0.002
RR_{1473}	%/min	0.44	0.01	0.13	0.001	0.70	0.012
S value	kPa x K	139	37.9	589	102.1	434	12.8

[a]Standard Deviation

Regarding the softening start temperature ($T_{10\%}$), low basicity materials softened at lower temperatures. The acid pellets showed the lowest softening start temperature (1340 K), followed by the lump ore at 1376 K and by the sinter at 1423 K. The parameter $T_{50\%}$, temperature where 50% of contraction is attained, can be used as the end of softening and the interval $T_{50\%} - T_{10\%}$ is related with the width of the softening stage and the contraction rate. Despite acid materials starting to soften at a lower temperature, the wider softening interval ($T_{50\%} - T_{10\%}$) was obtained for the lump ore (206 K), followed by the sinter (105 K) and the acid pellets (83 K). A similar tendency can be seen for the rate of contraction, with the acid pellets showing the most negative slope, followed by the sinter and the lump ore.

The melt exudation stage is associated with the formation of the cohesive zone in the blast furnace, where the permeability of the ferrous burden decreases severely. The parameter T_{SCZ} is associated with the upper surface of the cohesive zone and is obtained by the temperature at which the pressure drop across the bed reaches 1 kPa. The acid pellet showed the lowest T_{SCZ} at 1502 K, indicating that the position of its cohesive zone in the reactor would be the highest among the materials tested. The sinter showed an

intermediated T_{SCZ} of 1577 K, followed by the lump ore at 1598 K. Regarding the ending of the cohesive zone (T_{ECZ}), that was the lowest for the acid pellet (1590 K), followed by the lump ore (1661 K) and by the sinter (1737 K). From those results, the thickness of the cohesive zone can be qualitatively estimated by $T_{SCZ} - T_{ECZ}$. The lump ore showed the smallest thickness (62 K), the acid pellet was intermediary (88 K) and the cohesive zone for the sinter was the thicker (164 K). Despite the relatively small cohesive zone thickness of the acid pellet, its maximum pressure drop (Pmax) was the highest (22 kPa) and occurred at 1541 K. In comparison, at 1617 K the lump ore showed a Pmax of 4.3 kPa similar to that of the sinter (4.4 kPa) at 1626 K. The S value represents the global pressure loss in the test and it is usually associated with the pressure drop of the cohesive zone. The best S value was obtained by the lump ore (139 kPa x K), followed by the sinter (434 kPa x K) and by the acid pellet with the worst permeability (589 kPa x K).

2.3.2. Reduction Behavior

Figure 2.5 shows the reduction degree (R.D.) and the rate of reduction (R.R.) of the iron-bearing materials as a function of temperature. A similar behavior of reduction can be seen for all materials studied. Three different regions were delimited in Figure 2.5 based on the existing reduction pattern and phenomena. Region R1 delimits the interval in which reduction occurs through gas/solid reactions. When the reducing gas was introduced in the experiment, the R.R. increased rapidly until reaching a point of maximum and immediately after started to slowly and constantly decrease with temperature. This slow decrease in R.R. might be related to the progress of reduction and metallic shell formation, which increases the path necessary for gas diffusion[23]. As the reduction of the iron oxides progressed, a more significant decrease in R.R. was identified, which was used to determine the transition between the regions R1 and R2.

At region R2, a sharp decrease in R.R. occurs due to the phenomena known as reduction retardation. According to Shigaki et al.[5], this phenomenon takes place when the liquid slag fills the pores by capillarity, leading to the densification of the iron shell, which limits reducing gas diffusion and consequently reduction. For the samples studied, reduction retardation took place first for the acid pellet at 1358 K (Figure 2.5-b), decreasing the

R.R. enough to completely cease reduction for a few moments. In comparison, reduction retardation occurred to a slightly smaller extent for the sinter and was rather low for the lump ore. The temperature of reduction retardation for the sinter and the lump ore were relatively similar, at 1463 and 1448 K, respectively.

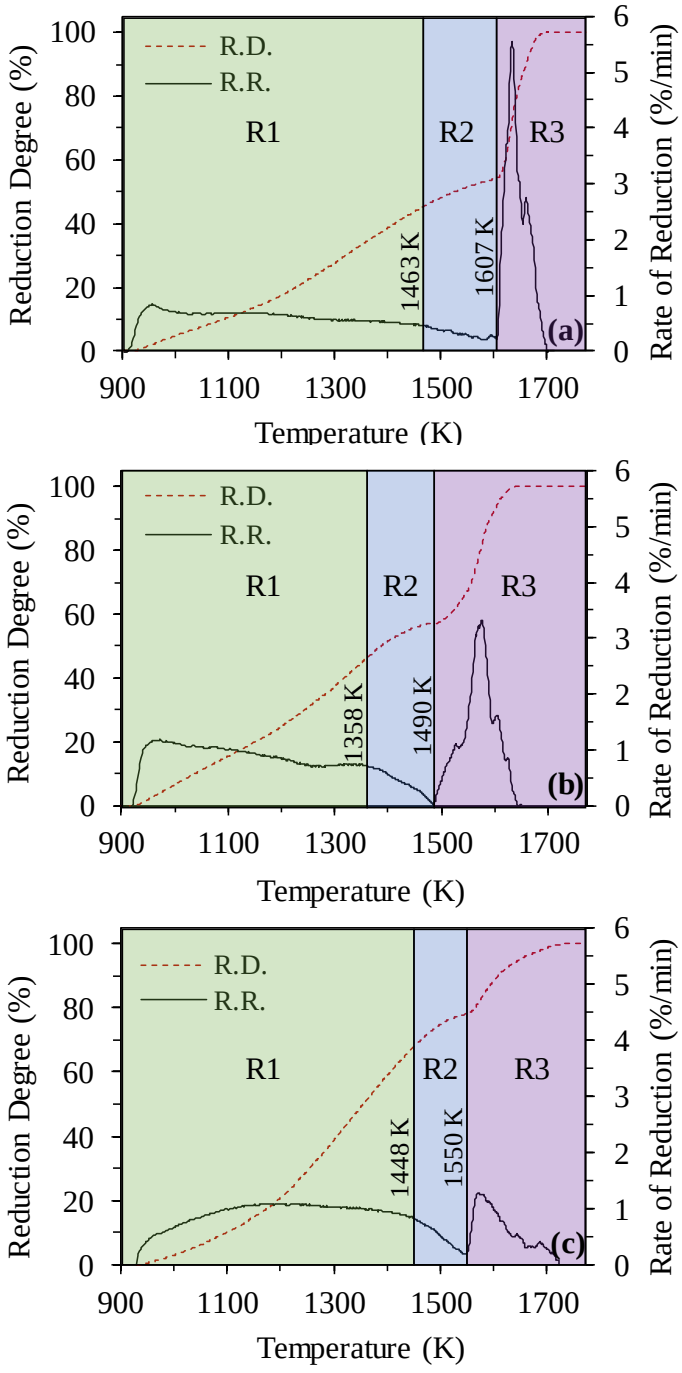

Figure 2.5. Degree and rate of reduction for the (a) lump ore, (b) acid pellet and (c) sinter. R1, R2, and R3 delimit the regions of gaseous reduction, reduction retardation and melt reduction.

The formation of liquid slag inside the particles is also important for the softening process. According to Bakker T.[4], softening and the consequent deformation of reduced materials are triggered due to the formation of slag, which causes a drastic change in microstructure. A comparison between the temperature of reduction retardation start (Figure 2.5) and the temperature of softening start ($T_{10\%}$, Table 2.3), reveals that those parameters were quite close for the sinter and the acid pellet. However, those temperatures were quite distant for the lump ore.

The third region of reduction (R3) is associated with the sharp increase in R.R. right after reduction retardation has reached its peak (lowest R.R. values). The increase in R.R. occurred due to melt exudation, allowing the contact of the liquid slag (rich in FeO), initially enveloped by the iron shell, with the reducing gas and the coke present in the experiment. The FeO in the slag is readily reduced by both reducing agents, producing high values of R.R. It can be seen that the peak of reduction in R3 was highest for the lump ore, intermediate for the acid pellet and the lowest for the sinter. In addition, using Equation 2.3, the rate of carbon consumption by melting reduction in R3 can be calculated and is presented in Figure 2.6-a. The profiles of the rate of carbon deposition/consumption were quite similar to those of the R.R. (Figure 2.5) in terms of temperature interval and intensity. Some carbon deposition (positive values) by the inverse of the Boudouard reaction was also seen at temperatures lower than those where melting reduction occurred, being similar for all samples. The deposition was verified to occur at the surface of the extremities of the Al_2O_3 tube, which are colder than the furnace heating chamber. The integration of the profiles showed in Figure 2.6-a, between the temperature range defined by region 3 (R3), gives the amount of carbon consumed by melting reduction (converted to kg of carbon per ton of iron-bearing material).

For the samples studied, the lower the R.D. at the beginning of region 3, the more intense the peak of R.R and the higher carbon consumption. The latter is related to the amount of ferrous slag that exuded from the particles, where greater quantities of melt might produce higher rates of reduction. However, this may not be true for basic iron-bearing materials. According to Nishimura et al.[18], due to the high basicity of sinter, melting reduction can

form solid $2CaO.SiO_2$ upon contact with metallurgical coke. This impedes further contact between coke and slag, suppressing melting reduction. In addition, for the sinter studied by Nishimura et al.[18], the formation of $2CaO.SiO_2$ was verified to occur slightly after the beginning of melting reduction by applying a thermodynamic model[20]. The relation between the degree of reduction and the amount of carbon consumed by melting reduction shows the importance of evaluating the phenomenon of reduction retardation and its mechanisms, especially for acid raw materials.

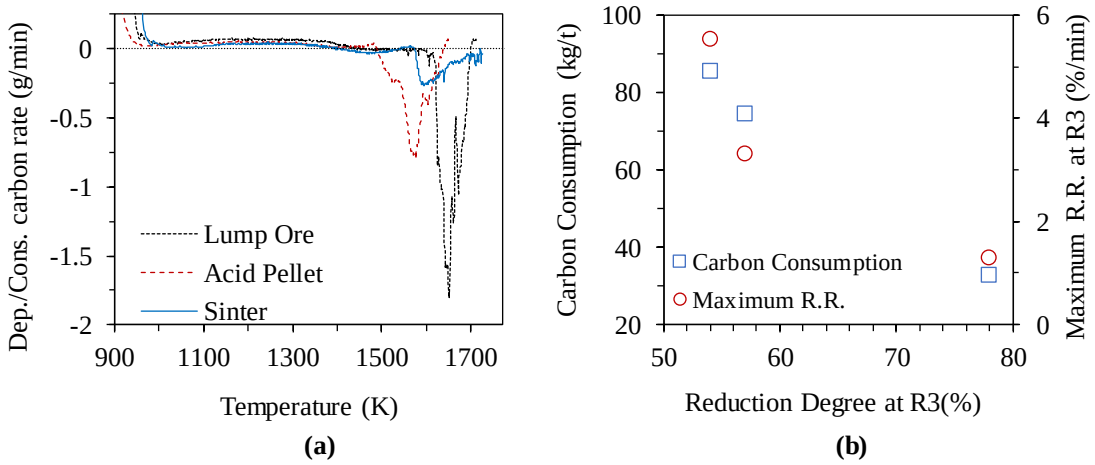

Figure 2.6. Rate of carbon deposition/consumption as a function of temperature and (b) the effect of reduction degree at the beginning of R3 on carbon consumption and maximum rate of reduction.

2.3.3. Softening and Melting Interrupted Tests

With the objective of investigating the evolution of the phase composition, microstructure and porosity of the iron-bearing materials at key instants within the softening and melting process, softening and melting interrupted tests were carried out. The temperatures selected for interrupting the tests were the following: pre-softening ($T_{pre\text{-}soft}$), $T_{10\%}$, $T_{50\%}$, and T_{SCZ}. With the exception of the $T_{pre\text{-}soft}$, determined at 1093, 1168 and 1250 K for the lump ore, acid pellet, and sinter, respectively, the other temperatures can be found in Table 2.3.

The test interruption at $T_{pre\text{-}soft}$ was carried out significantly before the identification of any deformation in order to obtain a partially reduced sample before the beginning of the

softening and melting process. At $T_{10\%,}$ softening is at its early stage and some deformation already occurred. The temperature $T_{50\%}$ provides a sample condition at the transition between the stages of softening and melt exudation, also being a contraction level within the range of reduction retardation. Finally, the temperature T_{SCZ} should provide a sample at the beginning of the melt exudation stage, before maximum pressure drop is attained.

2.3.3.1. X-ray Diffraction

Figure 2.7 shows the XRD profiles for the iron-bearing materials at the condition of as received (raw) and from the softening and melting interrupted tests. For all as received samples, hematite diffraction peaks were observed. Magnetite peaks were identified for the acid pellet and the sinter, while the latter showed wüstite in its composition as well. In addition, goethite, SiO_2, and silico-ferrite of calcium and aluminum (SFCA) were detected for the lump ore, the acid pellet, and the sinter, respectively.

With the progress of reduction from the raw material up to $T_{pre\text{-}soft}$, the diffraction peaks associated with hematite disappeared for the acid pellet, and those of the SFCA disappeared for the sinter. For the lump ore, goethite was completely eliminated although hematite was not fully reduced, and part of its reduction led to the formation of magnetite, wüstite, and iron. Similarly, for the sinter at $T_{pre\text{-}soft}$, diffraction peaks of hematite, magnetite, wüstite, and iron can be seen, together with the appearing of $2CaO.SiO_2$. For the acid pellet, the peaks associated with magnetite, wüstite, iron, and SiO_2 were identified.

At the temperature $T_{10\%}$, the iron oxides were mainly reduced to form wüstite and metallic iron for the acid pellet and the sinter. However, for the lump ore, hematite and magnetite still remained coexisting with wüstite and the iron, due to the lower reducibility of this material (see R_{1273} and R_{1473} at Table 2.3), and its low temperature $T_{10\%}$ (1093 K) in comparison to the other materials.

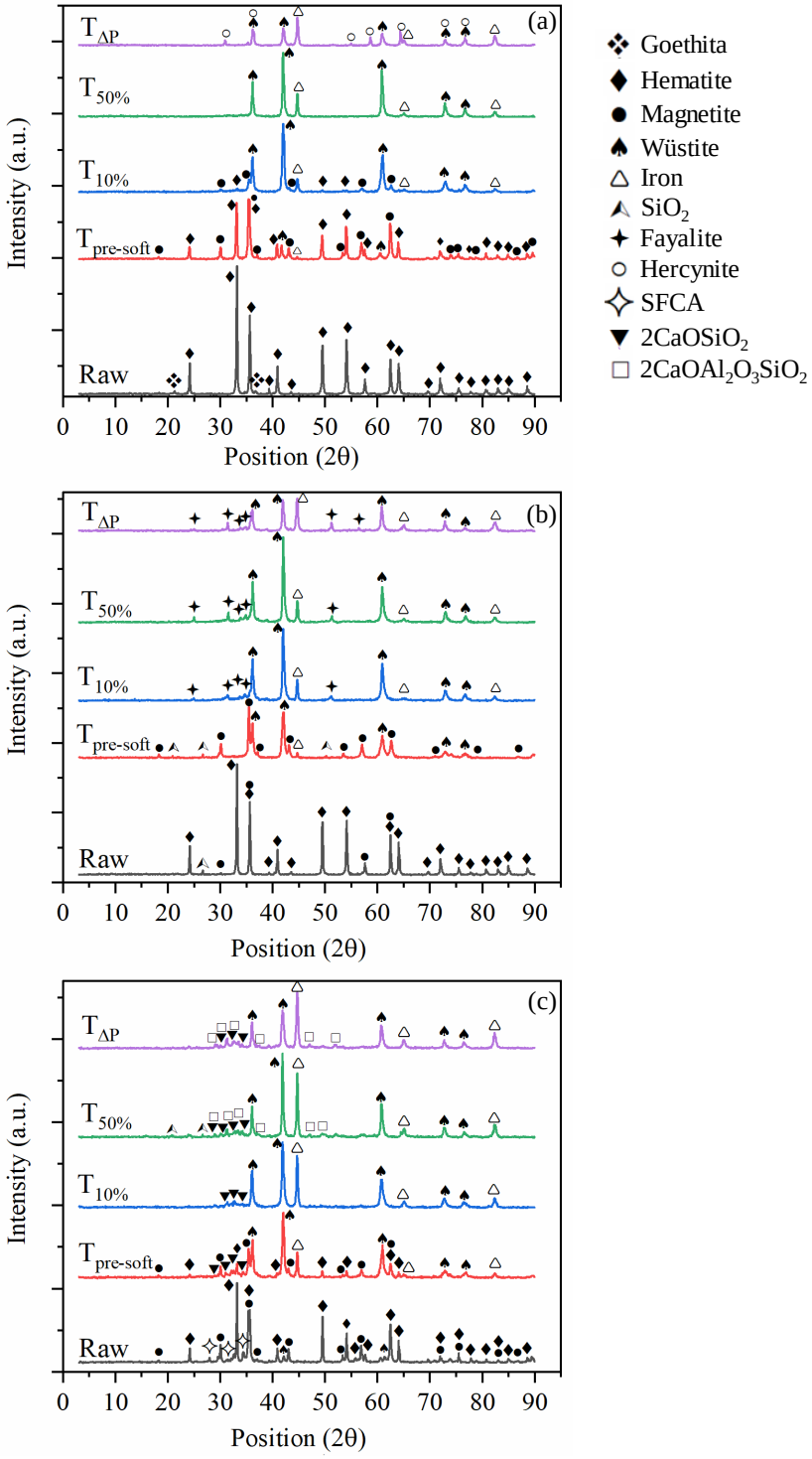

Figure 2.7. XRD profiles for the (a) lump ore, (b) acid pellet and (c) sinter as received and interrupted experiments.

At $T_{10\%}$, the formation of liquid in the material's microstructure is expected, since that is considered to be the trigger of deformation[4]. In this regard, the observation of a new phase between $T_{pre\text{-}soft}$ up to $T_{10\%}$ by using XRD was only seen for the acid pellet, where

the SiO_2 peaks disappeared giving place to those associated with fayalite (Fe_2SiO_4). The latter indicates that fayalite was the first liquid phase to be formed for the acid pellet. That is in accordance with other studies[10,12,24] focused on acid materials, where fayalite was identified as the first liquid to be formed during the softening and melting process. However, from the FeO-SiO_2 phase diagram, fayalite becomes liquid at 1450 K, which is rather higher than $T_{10\%}$ of the acid pellet (1340 K). The lower temperature of fayalite formation in commercial iron-bearing materials is usually associated with the presence of alkalis[10,12,24]. In comparison, the formation of new phases was not seen for the lump ore and the sinter. For the latter, the phases observed at $T_{10\%}$ alone are not conclusive to estimate slag formation.

From $T_{10\%}$ up to $T_{50\%}$, the lump ore reduced further leading to the disappearance of the hematite and the magnetite, remaining just wüstite and metallic iron. For the sinter, once more, $2CaO.SiO_2$ were identified and new peaks associated with $2CaO.Al_2O_3.SiO_2$ and free SiO_2 appeared. The formation of $2CaO.Al_2O_3.SiO_2$ for a sinter was also observed by Hayashi et al.[2] at temperatures above 1473 K ($T_{50\%}$ equal to 1523K). The X-ray diffractograms for the acid pellet at $T_{50\%}$ and $T_{10\%}$ were almost identical.

Finally, at T_{SCZ} melt exudation occurs and some changes in slag composition could occur due to the slag reduction. For the lump ore, Hercynite ($FeAl_2O_4$) was identified after the beginning of melt exudation. In the case of the sinter, the only difference between $T_{50\%}$ and T_{SCZ} was the disappearing of SiO_2, while once more the acid pellet showed no significant alteration.

2.3.3.2. Density and Porosity

The evolution of the true and apparent density of the iron-bearing materials and its products from the interrupted experiments are shown in Figure 2.8. First, regarding the true density (Figure 2.8-a) of the raw materials, which is related to the materials composition without any pores, the lump ore was the densest material, followed by the acid pellet and by the sinter. Those results are in accordance with the gangue content of each material presented in Table 2.1. As for the apparent density, the lump ore was once

again the material with the highest density, followed by the sinter and the acid pellet. The apparent density gives an indication of materials porosity, where the lower the apparent density the higher the porosity.

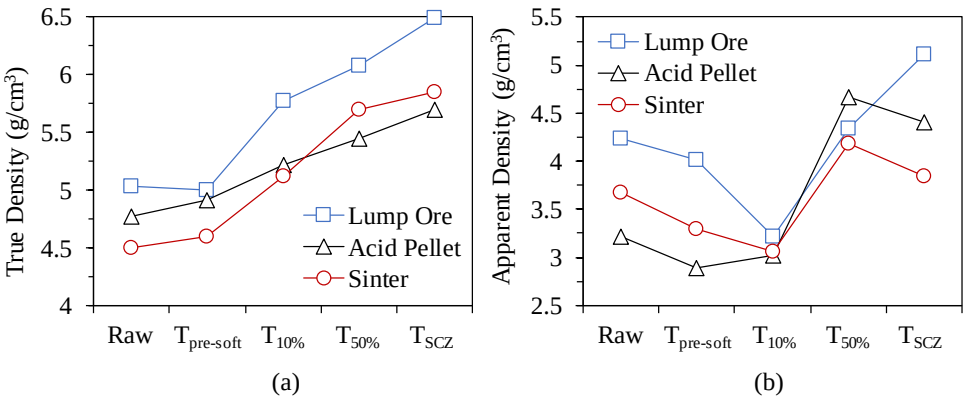

Figure 2.8. Evolution of true (a) and apparent (b) density for the iron-bearing raw materials and its interrupted products.

As the temperature of the interrupted products increased, the true density of all materials increased, which is related to the progress of reduction already shown in Figure 2.7, i.e., the formation of metallic iron and iron oxides with lower oxygen content. Additionally, from $T_{50\%}$ to T_{SCZ}, the sinter presented higher true density than the acid pellet. Moreover, all materials apparent density decreased down to a minimum at $T_{10\%}$ probably due to an increase in porosity from reduction. From that point on, samples apparent density started to increase up to $T_{50\%}$. For the samples interrupted at T_{SCZ}, apparent density increased for the lump ore but decreased for the sinter and acid pellet. The decrease in apparent density from $T_{50\%}$ to T_{SCZ} may be related to the melt exudation and the creation of porosity from the evolution of gas from melting reduction. The latter may vary from sample to sample according to each slag type, basicity, and viscosity.

Complementary to the density results, Figure 2.9 presents the variations in closed, open and total porosity of the raw materials and its interrupted products. With respect to the raw materials, open and total porosity was the highest for the acid pellet, while the sinter showed the highest volume of closed pores. The total porosity of the sinter and the lump ore were relatively similar, with the lump and the sinter showing the lowest percentages of closed and open porosity, respectively.

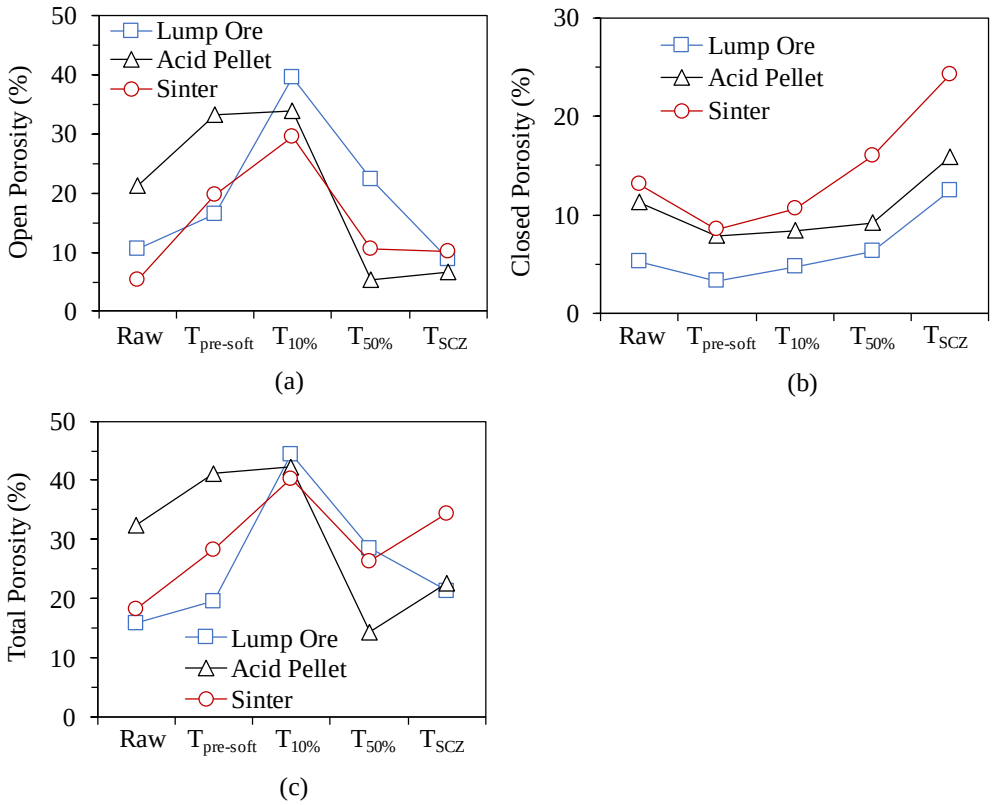

Figure 2.9. Evolution of (a) open, (b) closed and (c) total porosity for the iron-bearing raw materials and its interrupted products.

From the interrupted samples, a similar trend can be seen for all iron-bearing materials regarding the three types of porosity. First, as reduction progresses up to $T_{10\%}$ (Lump: 1376 K; Pellet: 1340 K; Sinter: 1423 K), a significant increase in open porosity (Figure 2.9-a) was observed for all materials, which also lead to an increase of its total porosity (Figure 2.9-c). The open porosity increased by 29.0, 12.6 and 24.3 percentage points (PP) for the lump, pellet, and sinter, respectively. This is probably related to the removal of oxygen from the reduction of iron oxides, opening the structure of the particles, and even the formation of cracks due to reduction degradation. However, except for the sinter, such an increase in open porosity did not cause a rise of R.R. (region R1, Figure 2.5) but may have increased the diffusion distance for the gas to reach the reaction interface, thus decreasing the rate of reduction. At the same time, a decrease in closed porosity was identified from raw to $T_{pre\text{-}soft}$, which after turned to increase slightly up to $T_{10\%}$. It is thought that as reduction occurs, part of the closed pores opens and becomes accessible by the gas, leading to an increase in open porosity at $T_{pre\text{-}soft}$. At $T_{10\%}$ the formation of

liquid slag in the microstructure of particles may create new closed pores depending on liquid's mobility.

When advancing from $T_{10\%}$ to $T_{50\%}$, a quite sharp decrease in open porosity was observed for all materials, which for the acid pellet declined by 28.6 PP. In comparison, the sinter and the lump open porosity diminish by 19.1 PP and 17.3 PP, respectively. A similar trend was observed by Shigaki et al.[5] for a dolomite pellet and in part explains the phenomenon of reduction retardation (region R2 at Figure 2.5), where materials that presented a higher extent of reduction retardation showed a greater diminishing in open porosity. From that, the pores connected with the particles' surface become closed and little reducing gas was capable of reaching the iron oxides, thus decreasing the rate of reduction. Regarding closed porosity, a further increase can be seen for all samples, probably by the same reasons already mentioned (due to liquid slag formation). The variation of total porosity followed the changes in open and closed porosity.

From $T_{50\%}$ to T_{SCZ}, the exudation of melt from particles' core to the bed affected samples differently. The open porosity of the sinter and the pellet changed slightly, while it decreased further for the lump ore. Concomitantly, the closed porosity of all samples increased. The slag exudation contributed significantly to diminish the porosity of the lump ore, closing the pores that remained open at $T_{50\%}$. In comparison, that effect was little pronounced for the sinter and acid pellet. Independently of the little open porosity at T_{SCZ}, the R.R. at region R3 increases sharply due to the melting reduction of the FeO rich slag.

2.3.4. Microstructure Evolution

The evolution of materials' microstructure was investigated using RLM and SEM. The RLM images of the peripheric and core part of particles are shown in Figures 2.10 and 2.11, respectively. From the raw samples, the distinct structures corresponded to each material can be seen. The lump ore and the pellet are majorly hematite, while the pellet also showed some quarts grains. The sinter presented some relict hematite, magnetite and SFCA. From the samples interrupted at $T_{pre\text{-}soft}$, reduction can be identified due to the

change in samples relief in comparison to the raw condition. Also, the periphery area (Figure 2.10) of the materials ($T_{pre\text{-}soft}$) appeared to be slightly more porous than the particles' cores (Figure 2.11). The microstructure of the lump ore was visually denser than the other materials, with the pellet and the sinter showing overall thinner walls and bigger pores. In pre-softening, the sinter was the only material with a significant layer of metallic iron (I) at its periphery. For the acid pellet, mostly wüstite (W) was observed for the periphery and core regions, with some dispersed SiO_2 (Q) particles and very little magnetite (M). Moreover, a wüstite layer was identified at the lump periphery forming a well-defined interface with the magnetite core. A similar interface can also be found at some sinter particles' cores. The observation of such interfaces confirms that reduction occurred according to the shrinking core model.

From the samples interrupted at $T_{10\%}$, all materials developed a clear metallic iron layer at the periphery region. Additionally, for the acid pellet and the sinter, some wüstite and slag (S) were found interspersed between metallic iron (Figure 2.10), with no apparent change of those individual structures in comparison to $T_{pre\text{-}soft}$. In contrast, the wüstite structure clearly changed for the sinter's core (Figure 2.11) and both regions of the acid pellet (Figure 2.10 and 2.11). Such a change is related to the formation of a liquid phase, generating a structure comprised of pseudo-globular wüstite shaped grains with discrete melt regions (slag-S) located in between the wüstite. It is clear from the XRD analysis that the slag phase formed for the pellet consists of fayalite from the assimilation of SiO_2 (Figure 2.7-b). However, the first melt is not clear for the other samples yet.

The pseudo-globular wüstite/slag structure appears to be in its initial stage of formation, once the melt regions are somewhat unconnected from one another. The latter is consistent with the stage of interruption of samples at $T_{10\%}$, where it is expected that limited quantities of melt would have been formed, thus triggering deformation. According to Bakker et al.[4], the liquid generated between the wüstite render the structure mobile, with the liquid acting as a lubricant, allowing particles to deform. It should also be considered that some bed deformation might have occurred due to the accommodation of the particles and even due to reduction degradation. This may explain why the lump ore did not present a marked change of microstructure between $T_{pre\text{-}soft}$ and $T_{10\%}$.

Additionally, even with the formation of liquid slag for the acid pellet and the sinter, the iron periphery remained rather porous. The latter agrees with the increase of open porosity of samples up to $T_{10\%}$ (Figure 2.9-a) and it appears that wüstite and the liquid slag retained a shape similar to that from $T_{pre\text{-}soft}$.

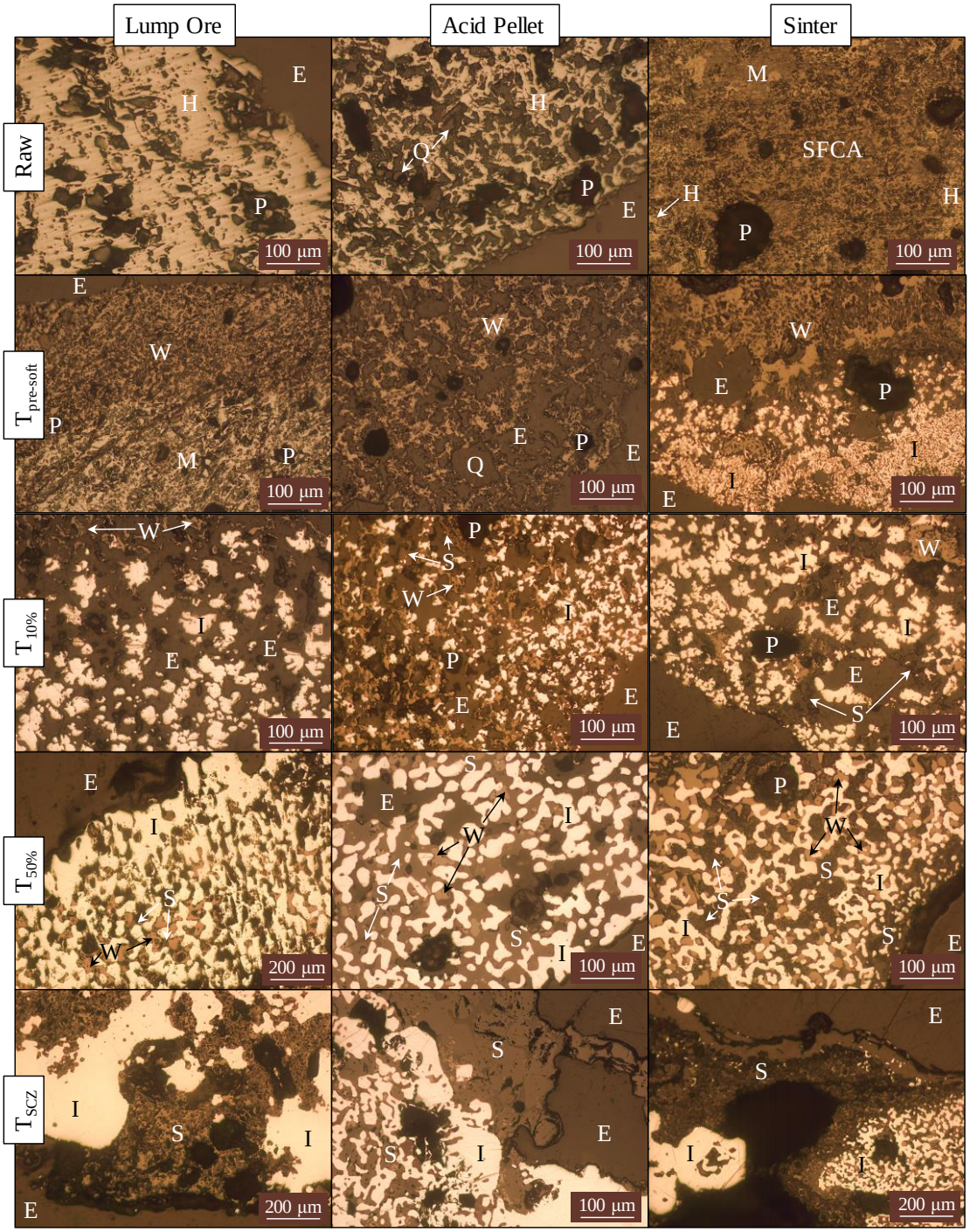

Figure 2.10. Microstructure evolution observed under RLM for the peripheric regions of lump ore, acid pellet and sinter particles from the interrupted softening and melting experiments. E: epoxy, P: pore, M: magnetite, W: wüstite, I: metallic iron, Q: quartz and S: slag.

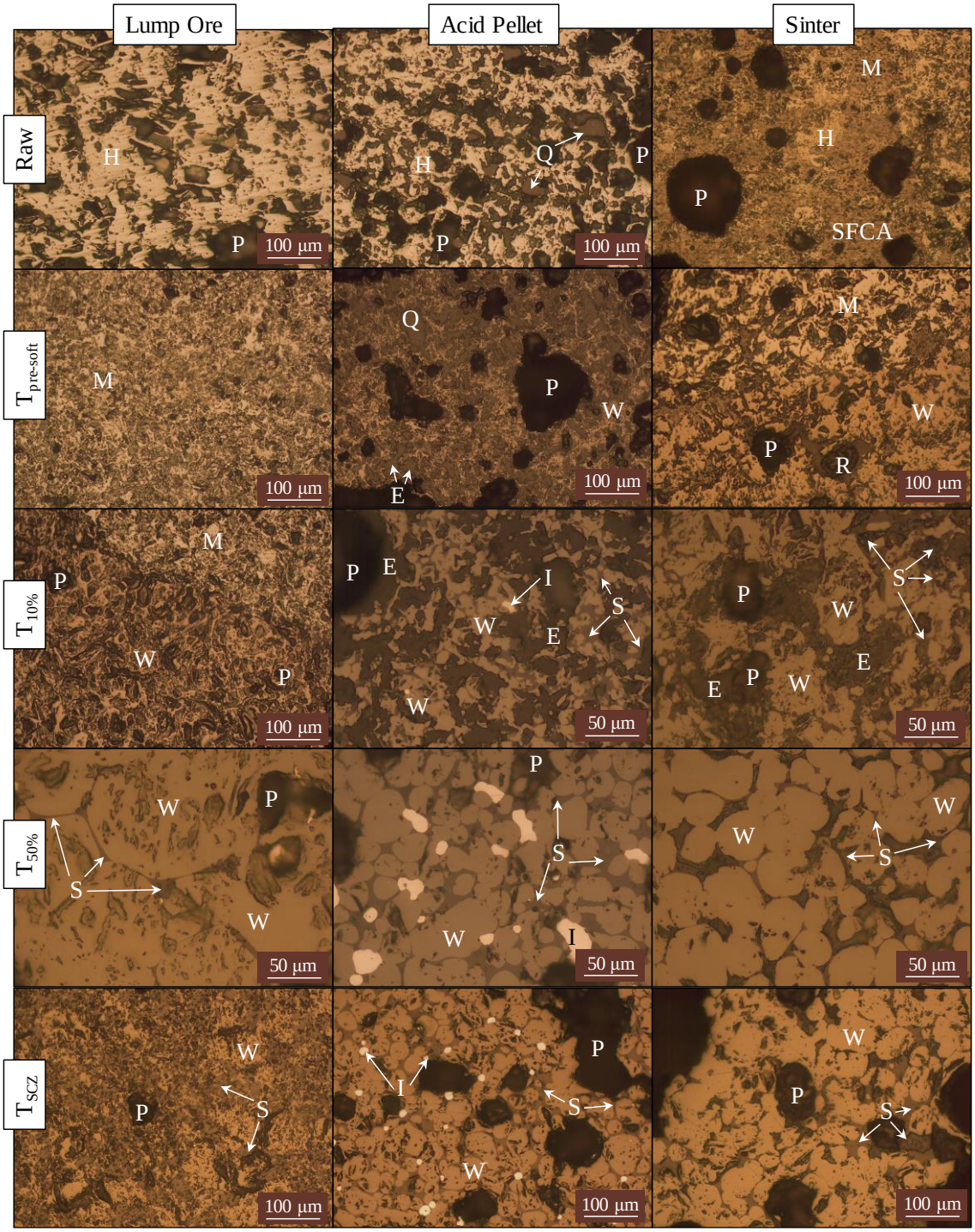

Figure 2.11. Microstructure evolution observed under RLM for the core regions of lump ore, acid pellet and sinter particles from the interrupted softening and melting experiments. E: epoxy, P: pore, M: magnetite, W: wüstite, I: metallic iron, Q: quartz and S: slag.

The evolution of the microstructure from $T_{10\%}$ to $T_{50\%}$ was remarkable for all materials. At the core regions (Figure 2.11-$T_{50\%}$), the samples developed the mixed structure of wüstite and slag. The shape of the wüstite changed from pseudo-globular to globular, which was surrounded by well-connected the liquid slag. The spheroidization of wüstite is considered to be caused by the melting of the slag surrounding wüstite[25]. Furthermore, the previous ($T_{10\%}$) acid pellet and sinter core microstructure suggest that coalescence of the wüstite/slag occurred in order to form the present structure. Moreover, from qualitative analysis, the wüstite globules were significantly bigger for the lump ore, which also showed very thin slag areas at the contours. According to Bakker et al.[4], the amount of slag also affects the deformation rate of the liquid/wüstite structure, where the bigger the amount of liquid the higher the deformation rate. In that sense, it can be assumed that the size of the wüstite globules is inversely proportional to the amount of liquid phase. From the RLM images in Figure 2.11 ($T_{50\%}$), it can be estimated that the wüstite globules were bigger (and vice versa for the liquid phase) in the following descending order: lump ore, sinter, and acid pellet. That is in agreement with the rates of contraction obtained in the softening and melting experiments (Figure 2.4), which can be indirectly seen from the difference between $T_{50\%}$ and $T_{10\%}$ (Table 2.3).

Regarding the peripheric regions of samples interrupted at $T_{50\%}$ (Figure 2.10), the thickness of the metallic iron layer significantly increased with the progress of reduction. In comparison with the particles' periphery at $T_{10\%}$, wüstite and large amounts of slag now fill up the spaces between the iron fingers, especially for the sinter and the acid pellet. The shell structure of the lump remained overall less clogged with slag than the other samples. It is believed that as the temperature rises from $T_{10\%}$ to $T_{50\%}$, consequently increasing the amount of liquid phase[2], the phenomenon of slag transfer occurs filling the iron shell porosity. That also explains the increase in closed porosity at $T_{50\%}$ (Figure 2.9-b), with slag transfer from the core to the shell leaving some porosity behind. According to Bakker et al.[4], this transfer is surface energy-driven in the direction of minimizing the free surface area of the iron. The slag transfer phenomenon explains, for all samples, the marked decrease in open porosity observed from $T_{10\%}$ to $T_{50\%}$ (Figure 2.9-a) and thereby the phenomenon of reduction retardation (region R2 - Figure 2.5). The

less clogged shell structure of the lump ore is also in agreement with reduction retardation occurring to a lower extent for this sample.

From the temperatures $T_{10\%}$ and $T_{50\%}$ (Table 2.3) and the temperature range delimited by reduction retardation (R2, Figure 2.5), it can be drawn that slag transfer and hence reduction retardation might happen in a more or less gradual fashion. Especially for the acid pellet and the sinter, the transition of R.R. from regions R1 to R2 is quite clear. Comparing the temperature where R2 starts and $T_{10\%}$, and considering that the rising of temperature leads to an increase of liquid fraction[2], it can be inferred that a bigger amount of liquid phase than that existent at $T_{10\%}$ is necessary for slag transfer to start. Beyond that, slag transfer and reduction retardation will both increase with temperature until the beginning of melt exudation.

It is interesting to see that besides part of the melt being exposed to the surface of the particle at $T_{50\%}$, (Fig 10), melt exudation was not identified. As the temperature increased further up to T_{SCZ}, several rupture points on the particles' metallic shell could be identified and part of the previously slag entrapped in the metallic shell exuded to the outer surface. The morphology of the peripheric iron has also changed in some regions, presenting a quite dense and uniform aspect. According to the literature[4,5], part of the reduction retardation phenomenon consists of the densification of the iron shell due to the penetrated slag being reduced[4] or by iron sintering in the presence of a liquid phase[5]. This suggests that such a dense iron could have been formed between $T_{50\%}$ and T_{SCZ}.

Samples interrupted at $T_{50\%}$ and T_{SCZ} were also investigated using SEM-EDS. The phases observed on each condition were just about the same in terms of distribution and composition and thus, for practicality, just samples interrupted at $T_{50\%}$ will be shown. The elemental maps of lump ore, acid pellet and sinter are shown in Figures 2.12 to 2.14 and the average elemental composition of the represented marked areas is presented in Table 2.4. The elemental composition by the SEM-EDS analysis was based mostly on areas of interest (average of 5-10 individual areas) of individual phases and hence might not represent the exact composition but can be used for qualitative interpretation.

Table 2.4. Elemental composition of the phases marked in Figure 2.12 to 2.15.

Sample	Phase	Fe	Ca	Si	Al	Mg	P	O
Lump Ore	1-Iron	96.86	0.32	0.61	0.29	0.25	0.32	1.34
	2- Wüstite	82.31	0.35	0.33	0.67	0.30	0.27	15.78
	3-Fayalite	58.37	0.39	13.24	0.53	0.51	4.56	22.40
	4-Slag	42.22	0.38	0.99	31.60	0.53	0.36	23.93
Acid Pellet	1-Iron	96.81	0.31	0.34	0.35	0.37	0.34	1.48
	2- Wüstite	81.22	0.54	0.61	0.79	0.19	0.18	16.48
	3-Fayalite	52.87	2.17	18.11	0.51	3.42	0.12	22.80
	4-Slag	16.34	12.90	22.62	11.04	1.78	2.35	32.97
Sinter	1-Iron	95.63	0.40	0.62	0.48	0.46	0.34	2.07
	2- Wüstite	79.52	0.68	0.31	0.38	1.90	0.25	16.96
	3-Slag1	9.18	32.07	17.30	10.69	1.82	1.61	27.33
	4-Slag2	11.38	40.53	16.79	0.95	1.30	0.36	28.68
	Ternary Structure[a]	21.24	25.9	13.83	11.01	1.56	0.64	25.82

[a]Structure marked in red in Figure 2.15.

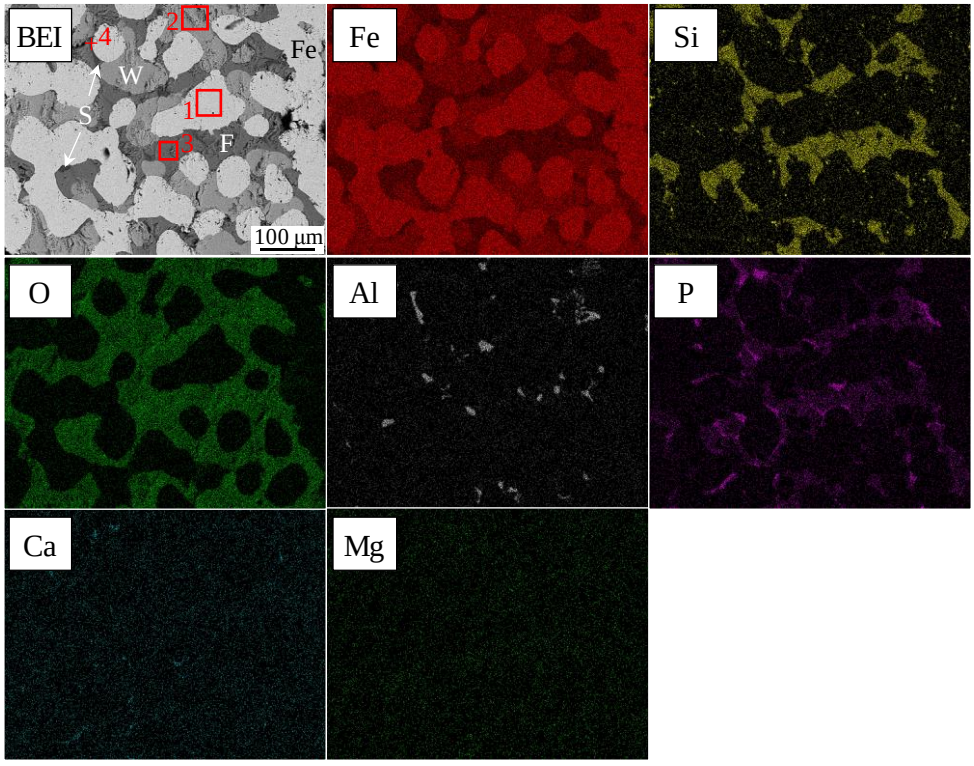

Figure 2.12. Element distribution from EDS maps for the lump ore $T_{50\%}$. BEI: Backscattering image; Fe: iron; W: wüstite; F: fayalite and S: slag.

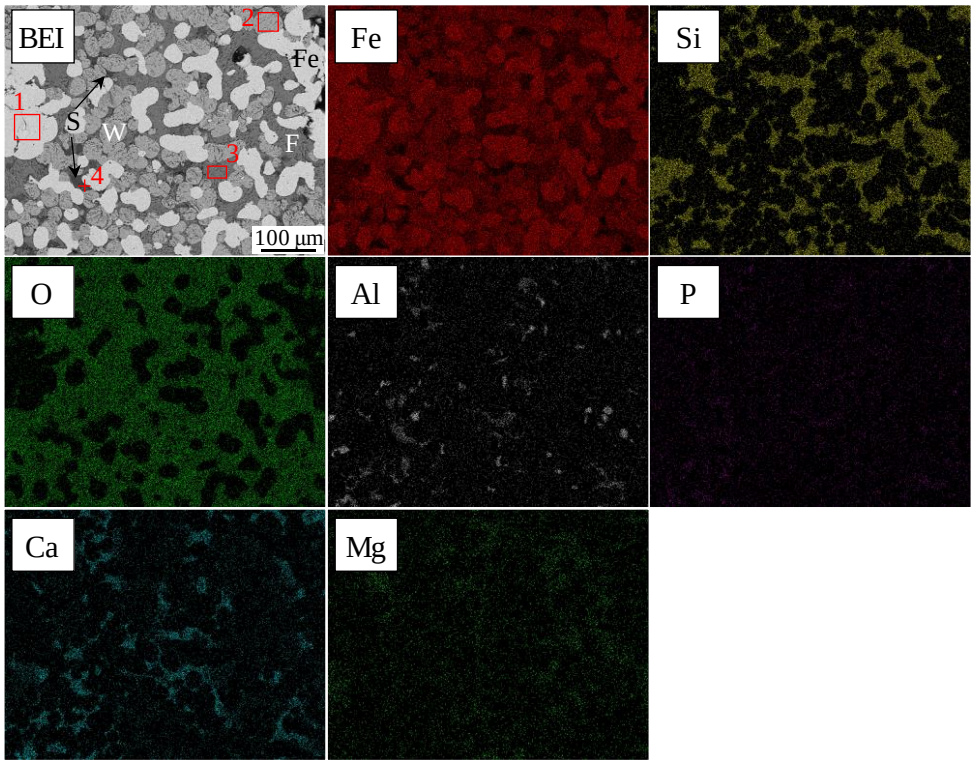

Figure 2.13. Element distribution from EDS maps for the acid pellet $T_{50\%}$. BEI: Backscattering image; Fe: iron; W: wüstite; F: fayalite and S: slag.

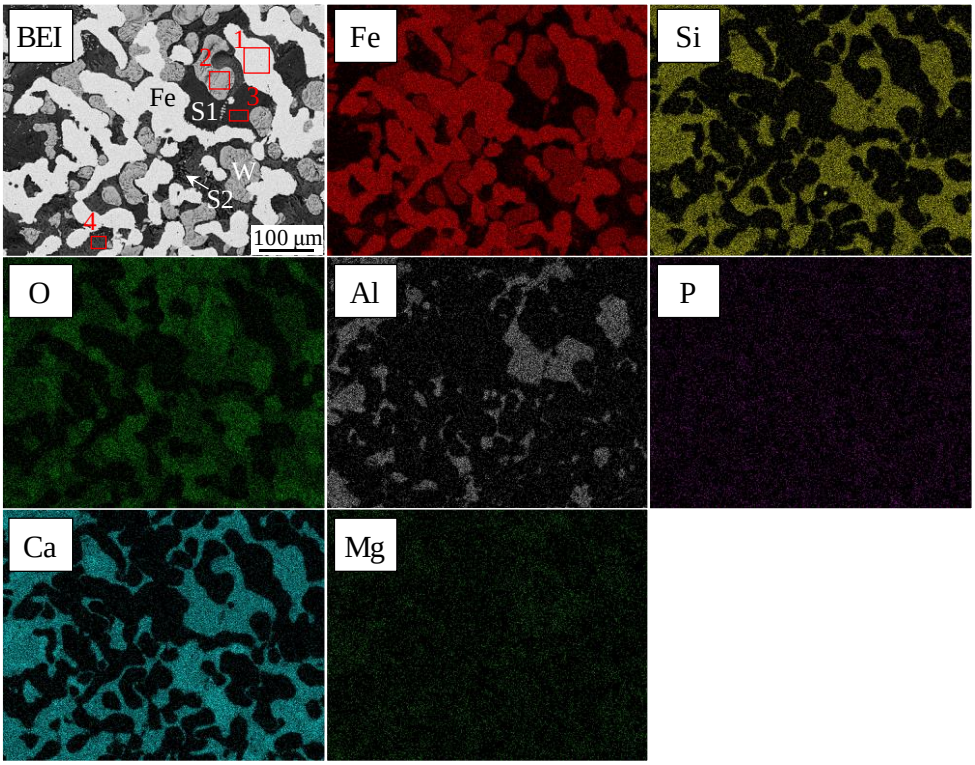

Figure 2.14. Element distribution from EDS maps for the sinter $T_{50\%}$. BEI: Backscattering image; Fe: iron; W: wüstite; S1: slag 1; S2: slag 2.

From these results, mainly four different phases were identified for each iron-bearing material. The metallic iron was pretty similar in shape (fingers) and composition (Table 2.4) for all cases. For the acid pellet and the lump ore, the similarity between the analysis of the distribution of Si, Fe and O (Figure 2.12 and Figure 2.13), as well as the elemental composition of the phase denoted by F, indicates that the first melt formed in the lump ore is also fayalite (identified in the pellet by XRD). That phase could not be identified in XRD probably due to its amount being inferior to the limit of detection of the technique. In addition, a comparison between fayalite elemental composition for these two materials shows that acid pellet fayalite is richer in Si, Ca, and Mg, while lump fayalite showed a significantly higher content of P. The concentration of P was only seen for the lump ore, although all samples had similar phosphorous content (Table 2.1). Besides the fayalite slag, two additional slag phases were observed for the lump ore and the acid pellet. The slag denoted as S in Figure 2.12 and Figure 2.13 is the darkest phase in the SEM. For the lump ore, the slag phase is mainly composed of Fe, Al, and O, and must be hercynite as this phase was found by the XRD for the temperature T_{SCZ}, slightly higher than $T_{50\%}$. In the case of acid pellet, slag was mainly composed of O, Si, Fe, Ca and Al.

In regards to the sinter, wüstite composition reveals that relatively little quantities of MgO were found in solid solution with wüstite. Moreover, by the relief of the slag phases, two types of slags could be identified in Figure 2.14, identified by S1 and S2. By the elemental compositions in Table 2.4 and the XRD profiles in Figure 2.7, slag S1 (smooth aspect) is $2CaO.Al_2O_3.SiO_2$ while slag S1 (relief texture) is $2CaO.SiO_2$, both containing some FeO in solid solution. Figure 2.15 shows in detail the different structures of the slags S1 and S2. In addition, both sinter samples interrupted at $T_{50\%}$ and T_{SCZ} presented a ternary eutectic structure of wüstite, $2CaO.SiO_2$ and $2CaO.Al_2O_3.SiO_2$. The average composition of areas marked in red is also shown in Table 2.4. According to Hayashi et al.[2], the ternary structure is composed of three phases with different FeO concentrations, where the ternary eutectic temperature of FeO, $2CaO.SiO_2$ and $2CaO.Al_2O_3.SiO_2$ is about 1573 K and thus eutectic melt has been formed at $T_{50\%}$ (1528 K) and T_{SCZ} (1577 K).

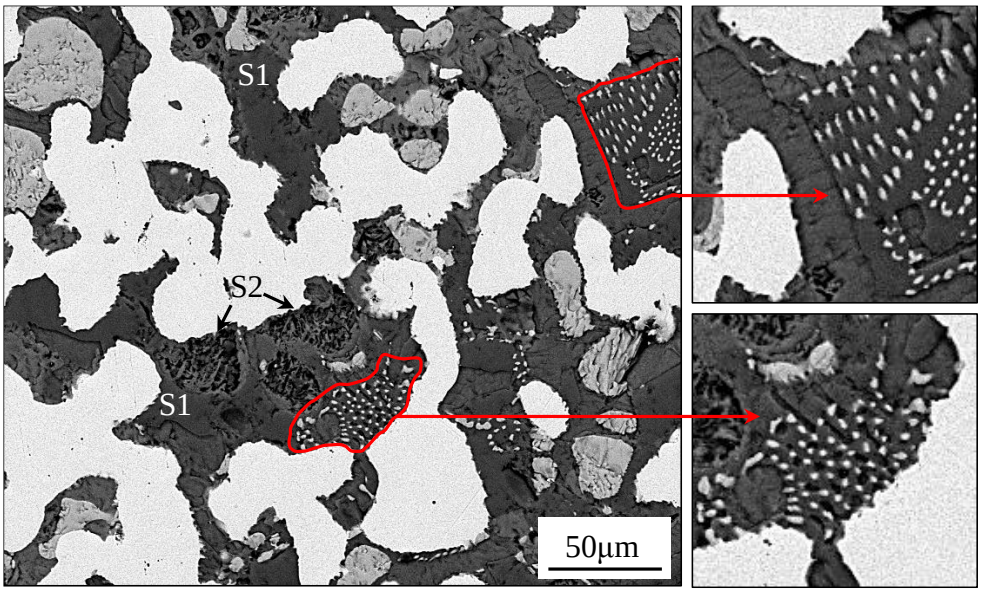

Figure 2.15. SEM image for the sinter T50% detailing both S1 and S2 slag structures and a ternary eutectic structure (red).

2.4. Conclusion

The behavior of reduction, softening and melting for samples of lump ore, acid pellet and sinter were presented and discussed in detail. The evolution of true and apparent density, porosity and microstructure of the materials were determined and associated with the known softening and melting phenomena as well as the high-temperature characteristics of each iron-bearing material. The major findings are as follows:

1. The reduction behavior of the samples was divided into three main regions accordingly to the occurring phenomena, comprising gas/solid reduction, reduction retardation, and melting reduction;
2. The extent of melting reduction and carbon consumption were inversely proportional to the degree of reduction of the iron-bearing materials at the beginning of the melt exudation stage;
3. The open porosity of the interrupted samples increased with the progress of reduction up to the beginning of softening ($T_{10\%}$). From that point on ($T_{50\%}$ and T_{SCZ}), a sharp decrease in open porosity was observed, leading to the phenomenon of reduction retardation;

4. A transition of microstructure associated with the formation of the first melt (softening) was observed for the acid pellets and the sinter at $T_{10\%}$. Prior to softening wüstite is continuous and presents a skeletal aspect, while after the formation of melt, wüstite appeared in discrete pseudo-globular areas interspersed by slag;
5. With the increase of temperature from $T_{10\%}$ up to $T_{50\%}$, the pseudo-globular/slag structure coalesced to form mainly globular wüstite grains in a well-connected slag matrix. The size of the wüstite globules and the thickness of the slag filling the wüstite boundaries varied between samples;
6. The phenomenon of slag migration was observed at $T_{50\%}$,where liquid slag migrated from the core to the iron shell periphery, sharply diminishing samples open porosity, while the closed porosity increased;
7. The ternary eutectic structure of wüstite, $2CaO.SiO_2$ and $2CaOAl_2O_3SiO_2$ was observed for the sinter samples $T_{50\%}$ and T_{SCZ}, heated up to 1528 and 1550 K, respectively.

Acknowledgments

The authors express gratitude to CAPES-PROEX, CNPq, and FAPEMIG for stimulating and supporting research.

2.5. References

1. P.F. Nogueira and R.J. Fruehan: *Metall. Trans. B*, 2004, vol. 35, pp. 829-838.
2. M. Hayashi, K. Suzuki, Y. Maeda and T. Watanabe: *ISIJ Int*, 2015, vol. 55, pp. 1223-1231.
3. T. Li, C. Sun, X. Liu, S. Song and Q. Wang: *Ironmaking Steelmaking*, 2017, vol. 45, pp. 755-763.
4. T. Bakker and R.H. Heerema: *Ironmaking Conf. Proc.*, 1998, pp. 1597-1608.
5. I. Shigaki, S. Shirouchi, K. Tokutake and N. Hasegawa: *ISIJ Int*, 1990, vol. 30, pp. 199-207.
6. P. Kaushik, R.J. Fruehan: *Ironmaking Steelmaking*, 2006, vol. 33, pp. 507-519.

7. G. Clixby: *Ironmaking Steelmaking*, 1980, 7, pp. 68-75.

8. V.J. Ritz, H.A. Kortmann: Ironmaking Conference Proceedings, 1998, pp. 1635-1654.

9. X. Liu, T. Honeyands, G. Evans, P. Zulli and D. O'Dea: *Ironmaking Steelmaking*, 2018.

10. Kemppainen, K. Ohno, M. Iljana, O. Mattila, T. Paananen, E. Heikkinen, T. Maeda, K. Kunitomo and T. Fabritius: *ISIJ Int*, 2015, vol. 55, pp. 2039-2046.

11. P.F. Nogueira and R.J. Fruehan: *Metall. Trans. B*, 2005, vol. 36B, pp. 583-590.

12. W.-T. Guo, Q.-G. Xue, Y.-L. Liu, X.-F. She and J.-S. Wang: *Ironmaking Steelmaking*, 2016, vol. 43, pp. 22-30.

13. L. Chen, Q.-G. Xue, W.-T. Guo, X.-F. She, J.-S. Wang: *Ironmaking Steelmaking*, 2016, vol. 43, pp. 458-464.

14. L. Chen, Q.-G. Xue, W.-T. Guo, X.-F. She, J.-S. Wang: Iron and Steel, vol. 51, pp. 15-21.

15. X. Liu, S. Wu, W. Huang, K. Zhang, K. Du: *ISIJ Int*, 2014, vol. 54, pp. 2089-2096

16. P. Kaushik and R.J. Fruehan: *Ironmaking Steelmaking*, 2006, vol. 33, pp. 520-528.

17. P. Kaushik and R.J. Fruehan: *Ironmaking Steelmaking*, 2007, vol. 34, pp. 10-22.

18. T. Nishimura, K. Higuchi, M. Naito and K. Kunitomo: *ISIJ Int*, 2011, vol. 51, pp. 1316-1321.

19. K. Ichikawa, J. Ishii, S. Watakabe and M. Sato: *ISIJ Int*, 2015, vol. 55, pp. 544-551.

20. I.V. Flores, A.L. Silva, N.C. Heck, M.C. Bagatini: Metall and Materi Trans B. 2019, In press.

21. J. Sterneland: Doctoral thesis, Royal Institute of Technology, Sweden, 2002, p. 233.

22. S. Jursova, P. Pustejovska, S. Brozova: Alexandria Eng. J., 2018, vol. 57, pp. 1657-1664.

23. L.V. Bogdandy, H.-J. Engell: *The reduction of iron ores: scientific basis and technology*. Springer Science & Business media, Berlin, DE, 2013.

24. M. Iljana, A. Kemppainen, T. Paananen, O. Mattila, E. Pisilä, M. Kandrokov and T. Fabritius: Int. J. Miner. Process., 2015, vol. 141, pp. 34-43.

25. K. Inoue, T. Ikeda and T. Uenaka: Tetsu-to-Hagané, 1982, vol.68, pp. 2431-2440.

Capítulo 3. Artigo B - A Thermodynamic Model Towards the Comprehension of Ferrous Burden Softening and Melting Using FactSage Macro Processing

Ismael Vemdrame Flores[a*], Aline Lima da Silva[b], Nestor Cezar Heck[c], Maurício Covcevich Bagatini[a]

[a]Metallurgical Processes Laboratory (LAPROMET), Federal University of Minas Gerais (UFMG), PO Box 31270-901, Belo Horizonte, Brazil.

[b]Metallurgical and Materials Department, Federal University of Minas Gerais (UFMG), PO Box 31270-901, Belo Horizonte, Brazil.

[c]Computational Thermodynamics for Metallurgy and Materials (NTCm Group), Federal University of Rio Grande do Sul (UFRGS), PO Box 91501-970, Porto Alegre, Brazil.

*Corresponding Author

The original final publication is available at springer website at the following link: https://link.springer.com/article/10.1007/s11663-019-01684-z.

Abstract

The softening and melting properties of iron-bearing materials play a decisive role in the formation of the cohesive zone, which greatly affects blast furnace gas flow distribution and heat-transfer efficiency. To improve the understanding regarding the evolution of condensed phases during reduction, softening and melting a thermodynamic model has been developed using FactSage™ thermodynamic software and macro processing. The model was constructed using a series of equilibrium stages and splitters to determine streams flow directions and to consider kinetic inhibitions. For all iron-bearing materials studied, the methodology proposed for modeling was capable of obtaining reduction degrees in very good agreement to its experimental data. The evolution of solid phases

was qualitatively comparable to the available literature, with Fayalite, Kirschsteinite, Melilite, and FeO as the main solid phases in equilibrium before slag formation. The comparison between the profiles of calculated slag mass fraction and experimental pressure drop showed a close relation between these properties. Moreover, the level of heterogeneity of each raw material may play a significant role in its results interpretation.

Keywords: Softening and Melting, FactSage, Macro Processing, Thermodynamics, Iron-bearing Materials.

3.1. Introduction

The blast furnace is a counter-current reactor where iron-bearing materials (lump ore, sinter, and pellets) and metallurgical coke are charged as discrete layers at the top of the furnace while preheated air and auxiliary fuels are injected through the tuyeres. During burden descent, the ferrous materials undergo reduction reactions, soften and melt. As a result, a region known as the cohesive zone is formed, which consists of a series of annular layers of semi-molten and impermeable ferruginous material, separated by coke layers (slits) that allow the gas to flow[1,2]. The cohesive zone influences the permeability and hence the gas and liquids distribution in the furnace, controlling process performance and productivity[3,4]. A narrow cohesive zone maximizes its permeability and hence productivity, while a zone positioned deep in the furnace minimizes heat consumption, lowering productions costs and provides the possibility to reduce variations in hot metal composition and temperature[5]. According to many authors[5-9], the high-temperature properties of the iron-bearing materials majorly control the width and position of the cohesive zone in the furnace.

To access the high-temperature characteristics of ferrous materials, softening and melting (S&M) under load tests are commonly used. In those experiments, a packed bed (usually sandwiched between two coke layers) is heated up to 1873K using a programmed, time-dependent variation of temperature, reducing gas composition and load[10]. The properties of the sample are obtained by the measurement of bed contraction, gas permeability, degree of reduction and temperature of the melts formation[10]. Interrupted S&M tests at

specific temperatures or contraction levels are also commonly carried out to determine the structural, physical and chemical characteristics of different samples. However, both types of S&M experiments cannot continuously access parameters such as phase composition, liquid ratio and slag viscosity, which are essential to elucidate the mechanisms responsible for ferrous materials S&M behaviors.

To overcome such experimental limitation and to obtain a more fundamental understanding of the S&M phenomena, studies assisted by thermodynamic commercial packages have been carried out. Kemppainen *et al.*[11] and Guo *et al.*[12] have computed phase diagrams designed to investigate the S&M of different types of pellets and sinter, predicting slag *solidus* and *liquidus* temperatures. Similarly, Liu *et al.*[13] have calculated primary slags *liquidus* temperatures and their viscosities based on the chemical compositions obtained from interrupted S&M experiments. Moreover, in the series of studies from Kaushik *et al.*[14,15], the authors used thermodynamics to predict the melting onset temperature and the slag fraction in comparison to samples bed contraction. Furthermore, Nishimura *et al.*[16] evaluated the softening, shrinking and melting reduction behavior of several ferrous materials using softening viscosity adjusted by thermodynamic equilibrium calculations. More recently, ICHIKAWA *et al.*[17] quantitatively estimated gas permeability of a softened sinter layer using liquid fractions from equilibrium calculations. However, despite the several studies, previous thermodynamic analyses do not provide a clear understanding on how the evolution of phases during reduction is related to important parameters such as pressure drop, which is closely related to blast furnace production; in fact, to the best of our knowledge, a more general, systematic and comprehensive approach to thermodynamically model S&M has not yet been carried out.

This work describes the current state of an on development thermodynamic model with the objective of better understanding the transformations and phenomena related to the S&M of different ferrous materials. For that, Factsage™ and macro processing were used to approach both indirect and direct reductions, with the addition of mathematical operators (splitters) based on experimental data to consider kinetic inhibitions. The

present model determines the solid and liquid phases evolution with temperature in comparison with softening and melting materials properties.

3.2. Thermodynamic Model

3.2.1. Model Description

The present model focused on the formation of the primary slag in the cohesive zone, which can be accessed experimentally by S&M tests. Primary slag is basically formed by FeO and gangue components from the iron-bearing materials[18] and thus, coke ash and other additives and fluxes were not considered in the present model. Nevertheless, in future studies, the investigation of the composition evolution from the primary slag to the bosh and final slags could be of interest.

Iron-bearing materials S&M can be understood based on the equilibrium state determination involving multi-component and multi-phase systems, in which iron oxides reduction and phase transformations are considered. In light of that, thermodynamic methods can be advantageous since they provide a common basis for complex chemical problems in multi-phase systems with various proportions and conditions[19]. In the present work, S&M was modeled based on the raw materials and test conditions reported by Nishimura *et al.*[16]. Despite many works on softening and melting of iron-bearing materials available in the literature, the work of Nishimura *et al.*[16] was the only one containing all the data necessary for the model. The equipment used by the authors, and also by several ironmaking industries, have a well-established methodology, giving reliable model input conditions and experimental results, which are essential to compare with the model output and to understand S&M.

The S&M experiments can be described as a vertical reactor into which a gas mixture and energy are continuously supplied to a fixed bed of ferrous raw material. Depending on the process temperature, various reactions will occur in the sample, and the products formed can be directed as (i) input into further reactions or (ii) eliminated from the system not participating in further reactions. Such a process can be understood as being

temperature-regulated, and to approach that the present model was divided into a series of sequential stages, each considered as an equilibrium reactor. According to the materials flow in the S&M experiments, condensed products (solids and liquids) will leave a given stage to react in neighboring stages while the gaseous products will exit the reactor. Each stage of equilibrium was defined with a predetermined temperature according to the temperature profile used in the S&M tests. As reported by Nishimura *et al.*[16], samples were submitted to reducing conditions from 1073 to 1823K, with heating rates of 10K/min from 1073 to 1273K and 5K/min from 1273 to 1823K. In the model, the experimental heating rates were used as temperature increments throughout those same temperature ranges. The temperature step can be seen as a parameter of progress in the simulations, allowing a direct relationship between temperature and the heating rates and gas flow rates. The choice of the temperature step determines the number of equilibrium stages available to cover the temperature range simulated, which consequently affects the computing time and the agreement between calculated and experimental data. The temperature step selected was adequate to approach the process in sufficient detail, without increasing the computing time excessively. Bigger temperature steps tend to produce results with high deviations from the experimental data, while smaller steps tend to increase the computing time without improving the model.

A schematic sequence of the equilibrium stages used can be seen in Figure 3.1 – a. As the simulation advances, both stage number and temperature increase. At first, the total amount of gas available (input gas phase, Figure 3.1 – a) for each stage, calculated from Nishimura *et al.*[16] gas flow and composition, was considered. At the same time, raw materials composition was input in the first stage of the model, and the condensed products equilibrated at a given stage were used as input into its subsequent one. At lower temperatures, only gaseous reduction occurred and as temperature increased and liquid slag was formed, melting reduction start, which led to the consumption of carbon.

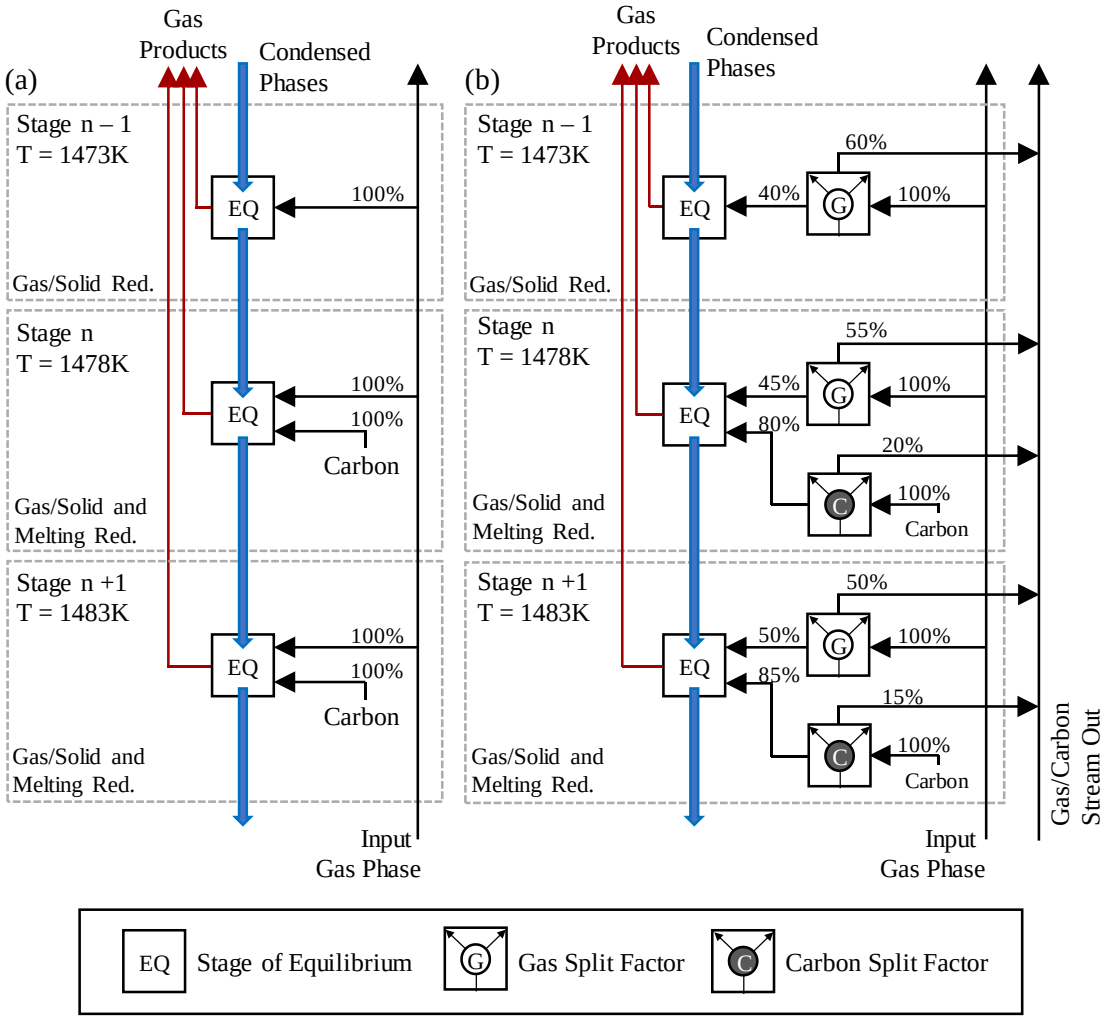

Figure 3.1. (a) Sequence of equilibrium (EQ) stages to thermodynamically model the S&M process and (b) the same sequence with the addition of split factors to consider kinetic constraints.

The use of a sequential multistage model (Figure 3.1 – a) allows for the implementation of additional operators, such as splitters. For example, if a countercurrent reactor would be modeled, splitters could be used to determine how the products formed (either by phase or amount) at a given region would flow (up or downstream) to react with neighboring areas. Additionally, splitters can be based on experimental data allowing to indirectly treat kinetic inhibitions by limiting the amount of a reacting material[20], like the reducing gas and carbon available at each stage. Splitters and other basic unit operators are commonly seen in process simulations, which interest has increased in recent years[20,21]. Splitters are of major importance to the present model since iron oxides reduction frequently does not achieve thermodynamic equilibrium. Kinetically, the rate of reaction

of a single ore will be determined by the total resistance generated by the following general steps[22]: (i) gas film resistance; (ii) diffusion resistance through the product layer (reduced oxide shell) and (iii) chemical reaction resistance at the metal-oxide interface. To deal with the kinetics of reduction, splitters were applied over the input gas phase at each equilibrium stage, limiting the amount of reducing gas that would interact with the condensed phases (iron oxides). That can be seen in Figure 3.1 – b, which schematically shows how the splitters were applied over the multistage model initially presented in Figure 3.1 – a. The splitters were calculated based on the divergence between the experimental reduction degree reported by Nishimura *et al.*[16] and the model results.

3.3. Thermodynamic Databases and Calculation Procedure

To carry out the equilibrium calculations and operations involved in the present model the method of Gibbs energy minimization was applied using the FactSage™ (version 7.1)[23]. In Gibbs energy minimization, no knowledge of a particular reaction mechanism is required to solve the problem. A stable equilibrium condition is reached when the Gibbs free energy of the system is at the minimum and the only input needed for this method is the elemental composition of the feed materials and the temperature/pressure conditions. A macro processing file containing a set of instructions for iterative calculations and loops was created to run with FactSage™ allowing its communication with Microsoft Excel spreadsheets to read input conditions, store results for further operations, export results, as well as calculating and applying splitters.

The computational flow diagram showing the operations used for the thermodynamic equilibrium calculations with the addition of splitters to consider kinetic constraints can be seen in Figure 3.2. In summary, the following steps were adopted in the calculation process: {1} initial conditions input; {2} equilibrium calculations between ferrous material and gas at each stage; {3} application of splitters (see Equation 3.1); {4} if melting reduction occurs, gaseous reduction is fully simulated until acceptable relative errors, the last set of gas splitters obtained are fixed and carbon is input at the stages in the melting reduction interval; {5} loop steps 2 to 4 until all the absolute relative errors between model and experimental[16] results are below 5%. In the calculations, the

equilibrated condensed phases at each stage are used as stream inputs for further calculations. The splitters to treat kinetic inhibitions are calculated according to Equation 3.1, where RD_{exp}^{T} and RD_{sim}^{T} represent the reduction degree at temperature T from experimental[16] and simulated results. Both reduction degrees were calculated according to Equation 3.2, where O_r^T is the oxygen removed from the material at a given stage and O_{total} as the total oxygen initially present in the iron oxides. Input gas phase splitters were limited to a maximum value of 1, which allowed all the amount of gas to react with the iron oxides. Carbon splitters were applied over the stoichiometric carbon necessary to reduce the remaining oxygen from pure gas reduction. The thermodynamic phase equilibria were calculated using the FToxid, FactPS and SGTE databases.

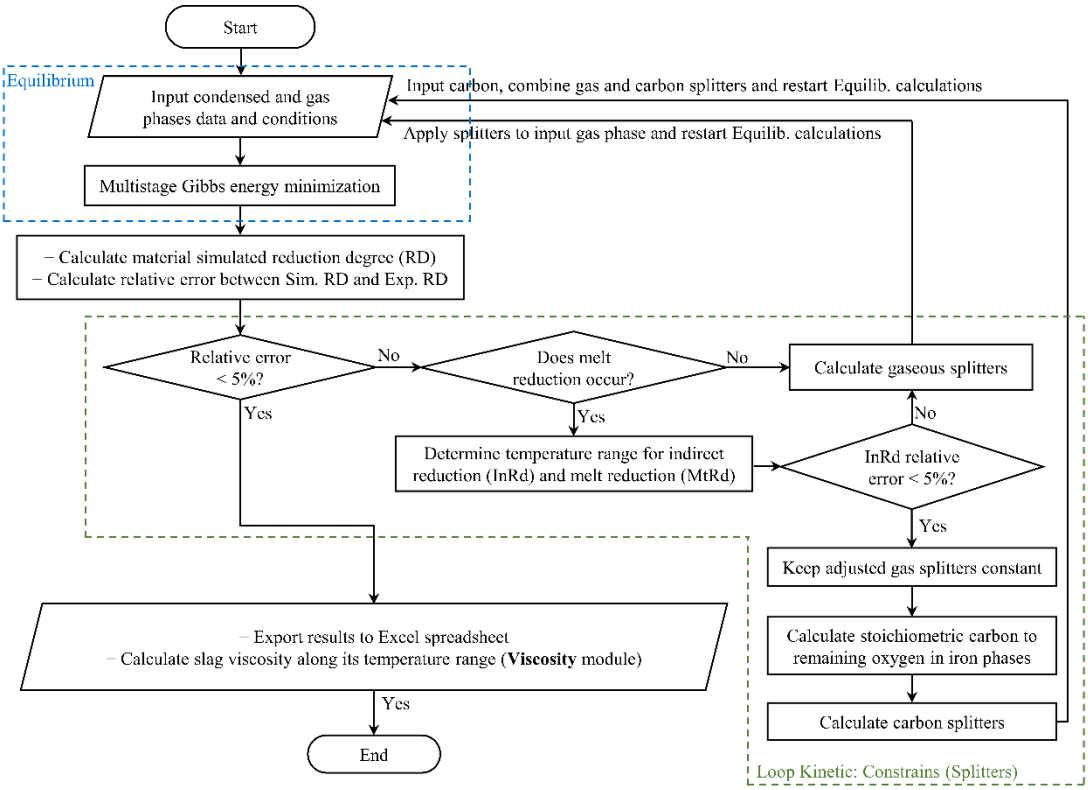

Figure 3.2. Computational flow diagram for thermodynamic calculations considering kinetic constraints (InRd = indirect reduction, MtRd = Melt Reduction).

$$\text{Splitter (input gas phase and carbon)} = \prod_{Iteration=1}^{n} {RD_{exp}^{T}}\Big/{RD_{sim}^{T}} \qquad (3.1)$$

$$\text{Reduction Degree}\left(\text{RD}_{\text{sim or exp}}, \%\right) = {O_r^T}/{O_{total}} * 100 \quad [3.2]$$

3.4. Results and Discussion

3.4.1. Thermodynamic Model Validation

To verify the accuracy of the developed model the ferrous raw materials reported by Nishimura *et al.*[16] were simulated, and the calculated results were compared with its respective S&M test results. Table 3.1 shows the chemical composition of the ferrous raw materials and its calculated elemental composition used as initial model input. To calculate the amount of oxygen in each material, the total iron (Fe_t) remaining after subtracting iron as FeO was considered as Fe_2O_3.

Table 3.1. Ferrous raw materials chemical composition, as reported by Nishimura et al.[16], and its calculated elemental composition used as initial model input.

	S&M Charge (g)	Chemical Composition (wt. %)						Basicity
		Fe_t	FeO	CaO	SiO_2	Al_2O_3	MgO	
Lump Ore	940	67.46	0.38	0.03	1.29	0.89	0.02	0.02
Acid Pellet	880	67.29	-	0.71	2	0.3	0.39	0.36
S-Fluxed Pellet*	891	65.7	0.57	2.61	2.28	0.62	0.06	1.15
Sinter	673	57.81	7.02	10.12	4.89	1.89	0.64	2.07

	Charge (g)	Elemental Composition (g)					
		Fe	Ca	Si	Al	Mg	O
Lump Ore	940	642.98	0.20	5.75	4.49	0.11	286.46
Acid Pellet	880	594.58	4.48	8.26	1.40	2.08	269.20
S-Fluxed Pellet*	891	588.78	16.71	9.55	2.94	0.32	272.70
Sinter	673	391.43	48.96	15.47	6.77	2.62	207.75

*Self-fluxed pellets

Figure 3.3 (a-c) shows the development progress of the model by comparing the experimental[16] and calculated reduction degrees. In the figure, the latter was obtained by using (a) exclusively thermodynamics, (b) thermodynamics with input gas splitters and (c) thermodynamics combining input gas and carbon splitters. The gray dotted lines in the figure delimit the maximum relative errors (±5%) adopted during the calculations.

As initially expected, all calculated reduction degrees obtained by thermodynamics alone (Figure 3.3 – a) highly overestimated materials experimental results because kinetic restrictions are not considered.

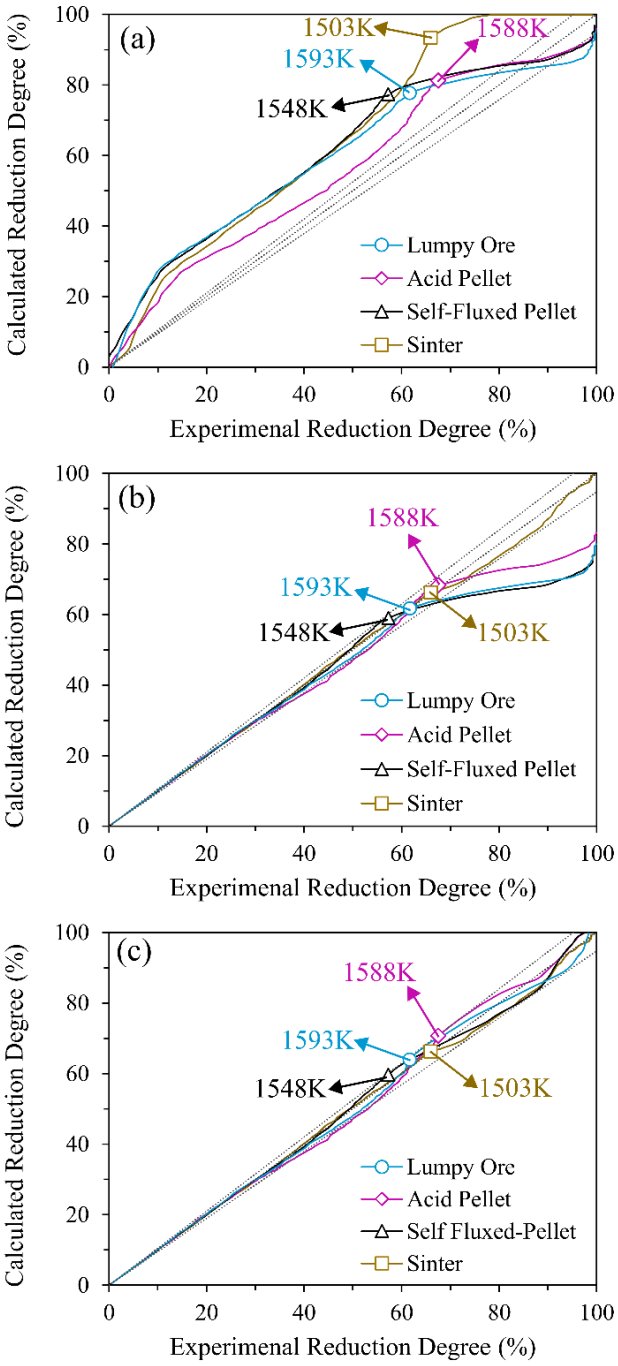

Figure 3.3. Comparison between experimental and calculated reduction degrees using (a) just thermodynamics, (b) input gas splitters and (c) both input gas and carbon splitters combined. Highlighted temperature identifies the starting of melting reduction

In comparison, from Figure 3.3 – b, it can be seen that applying splitters to limit the amount of reducing gas available at each equilibrium stage (Figure 3.1 – b), hence treating kinetics, significantly improved model accuracy. In especial, sinter results were in excellent agreement with measured data in the whole range of reduction. Nevertheless, input gas splitters were not sufficient to fully simulate iron oxides reduction. In the case of both pellets and the lump ore, the model underestimated the experimental data when experimental reduction degrees were above 60%, approximately.

To further improve the model, the reduction behavior of each material was analyzed according to the input gas splitters used in the results presented in Figure 3.3 – b. Fundamentally, splitters can be seen as temperature-dependent functions, shown in Figure 3.4 – a. Based on the variations on the experimental reduction degree from one stage to another, the smaller the value of the splitter, the lower the amount of reducing gas available for reduction, and higher the kinetic restrictions. In general, the different splitters varied between 0.25 and 0.7 from 1073 to 1273K, depending on the sample type and process of agglomeration. With increasing temperature, the rate of reaction and heat transfer are enhanced, consequently leading to an increase of all splitters up to its maximum allowing more reducing gas to be used at each equilibrium stage.

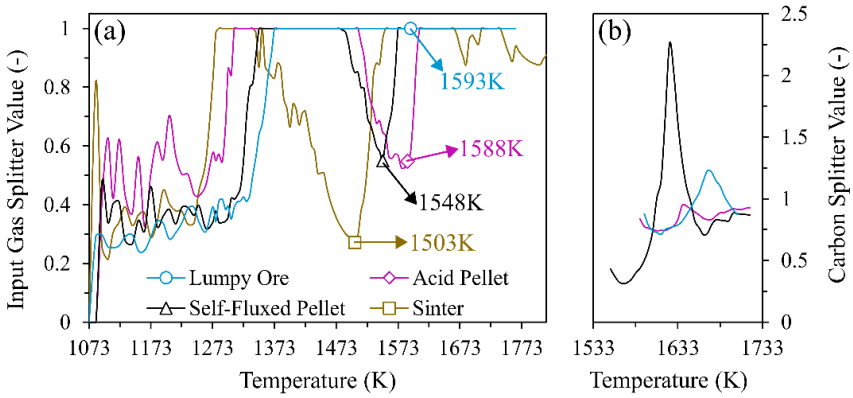

Figure 3.4. (a) input gas and (b) carbon splitters functions applied to the multistage thermodynamic model. Highlighted temperature identifies the starting of melting reduction

Two different reduction phenomena were identified by the input gas splitter functions presented in Figure 3.4 – a, namely reduction retardation and melting reduction. As the

reduction of iron oxides by a gas phase occurs topochemically, a structure comprised of a metallic iron shell enveloping an oxidic core (gangue and wüstite) is formed[5-7]. At temperatures slightly after the beginning of softening[24], sintering of the metallic shell takes place, blocking gas diffusion due to pores elimination, consequently causing reduction retardation[24,25]. The described phenomenon can be observed for both pellets and the sinter by the profile of the splitters (Figure 3.4 – a), which after reaching a maximum showed a downward trend down to a minimum point, thus limiting gas reduction. It can be seen that reduction retardation started earlier and was more significant for the sinter (1323K), while acid and self-fluxed pellets had a similar retardation behavior, although less intense than sinter, starting around 1498K. In comparison, the amount of reduction retardation showed by the lump ore was quite small, presenting no effect on its input gas splitter profile.

Furthermore, as temperature increases, particles' metallic shell weakens and the ferrous melt initially within the particles exudes filling the voids in the bed[5,6,26]. The ferrous melt is readily reduced when in contact with coke, which is commonly present in the S&M experiments, thus initiating melting reduction. For the materials being simulated, the temperatures where melting reduction took place (highlighted in Figure 3.3 and 3.4 – a) were identified by a sharp increase in the rate of reduction during S&M experiments[16]. It can be seen from Figure 3.4 – a that the indicated temperatures are similar to those where the slopes of the splitters shift, denoting the transition from reduction retardation to melting reduction. From the results presented in Figure 3.3 – b, after melting reduction started experimental reduction degrees were always higher than simulated results, even with maxed splitters, due to carbon not being considered in the calculations.

To input carbon in the simulations, temperatures of melting reduction were used to establish the reducing agents actuating during the S&M experiments. At temperatures lower than those of melting reduction, reduction was assumed to occur majorly by the gas phase, and the calculations were carried out with no carbon (Figure 3.3 – b). When melting reduction started carbon was added in the model, and both reducing agents were considered. The amount of carbon initially input in the model was calculated from the stoichiometric carbon necessary to remove the oxygen remaining in the iron oxides from

gaseous reduction. The final carbon content was then adjusted using splitters, which can be seen in Figure 3.4 – b. Differently from the input gas splitters, carbon splitters were not limited to a maximum value, since there wasn`t any experimental parameter available from Nishimura et al. [16] that could be used for that. In future studies, a balance of carbon can be carried out from the inlet and outlet gas analysis, allowing to estimate and limit the consumption of carbon due to melting reduction.

The results obtained by the complete thermodynamic model, *i.e.*, using gas and carbon as reductants, and splitters to indirectly treat kinetic constraints can be seen in Figure 3.3 – c. After carbon reduction was considered in the model, all samples were in good agreement with its experimental reduction degrees within maximum absolute relative errors of 5%. Carbon was not necessary to simulate sinter reduction. According to Nishimura *et al.*[16], the latter occurs due to the highly basic slag of sinter (CaO/SiO_2 = 2.07), which can form $2CaO.SiO_2$ (C_2S) upon contact with metallurgical coke. The formation of C_2S impedes further contact between coke and slag, suppressing melting reduction[16,25].

The good agreement obtained between calculated and experimental data ensure that the oxygen amount resulting from the model is quite similar to those obtained experimentally, and other types of data, such as solids composition and slag composition can be obtained with certain reliability. For future improvements regarding the model presented, the input gas splitters function could be derivated from raw-materials parameters, such as type (lump, pellets or sinter), basicity, porosity, and reducibility index with the auxiliary of a larger data bank and statistics/optimization methods.

3.4.2. Condensed Phases Evolution

Figure 3.5 (a–d) shows the overall reduction behavior, considering slag and metallic iron formation, of the simulated iron-bearing materials. The plots of oxide phases comprise all pure solid oxides commonly seen in iron-bearing materials and its possible solid solutions. A similar reduction trend can be seen for all iron-bearing materials simulated. Based on the S&M experiments from Nishimura *et al.*[16], iron oxides reduction started at

1073K. As the temperature increased, the reduction degree of all materials rose due to oxygen removal from the iron oxide phases. The formation of metallic iron was first observed for the sinter at 1278K, followed by acid pellets, self-fluxed pellets and the lump ore, respectively at temperatures of 1303, 1343 and 1363K. Those results agree with the reducibilities reported by Nishimura *et al.*[16], where the more reducible the material, the earlier metallic iron was identified. The carburization of metallic iron by solid carbon was not considered in the current model and thus liquid iron cannot be formed before 1811K. Accordingly, sinter was the only material to achieve such high temperatures, consequently forming liquid iron.

In what regards slag formation, liquid appeared first for the acid pellets (1383K), followed by the lump ore (1418K), sinter (1438K) and finally the self-fluxed pellets (1453K). The slag profile was very similar for the lump ore, acid pellets, and self-fluxed pellets, with a fast increase at the beginning until an approximately stable plateau, which lasted up to roughly 1573K where an abrupt rise in slag amount was seen. In comparison, sinter liquid slag showed a more smooth profile with similar rates (slope) of formation and reduction. Temperatures for slag formation were significantly lower than those where melting reduction took place, showed in Figure 3.3 and 3.4. This is in agreement with the fact that slag starts to form in the core of particles, being able to react with coke and reduce just after melt exudation occurs. More about the relation between the slag profile and the softening and melting phenomena will be discussed later.

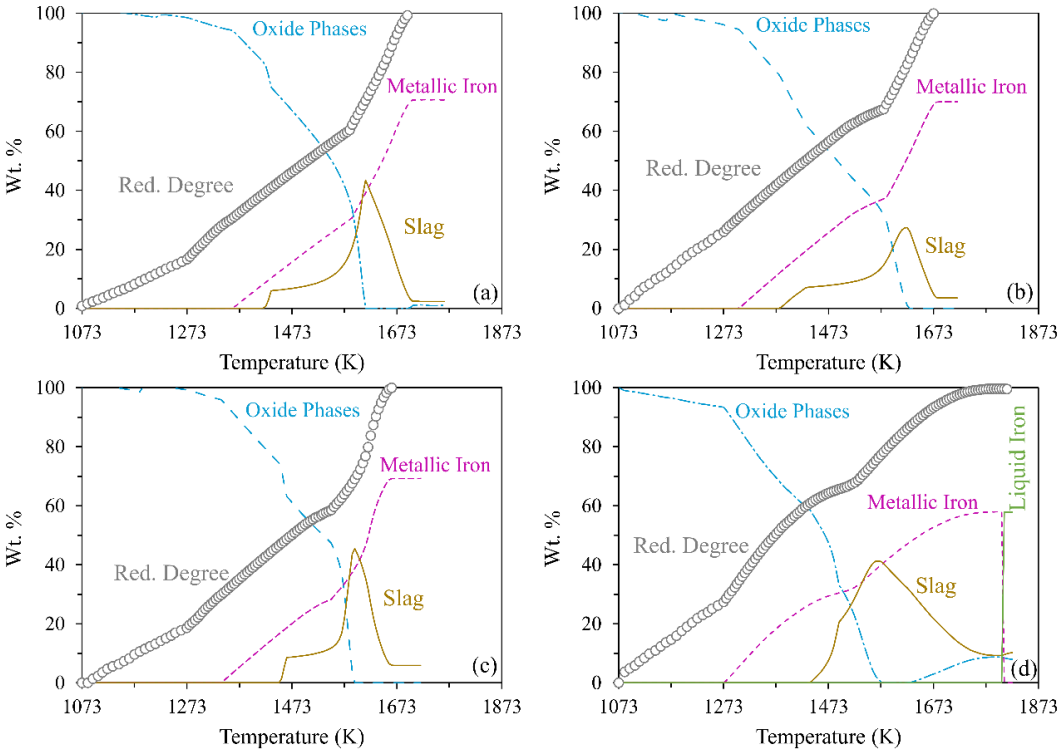

Figure 3.5. Evolution of major condensed phases in weight percentage calculated for the lump ore (a), acid pellet (b), self-fluxed pellets (c) and sinter (d) in relation to each material initial mass

Moreover, understanding the amount and composition of the solid phases present in iron-bearing materials is of importance since those are the precursors of melt and the solid relations will determine the temperatures of first melt formation[26]. In this sense, Figure 3.6 (a–d) shows the detailed composition of oxide phases obtained by the thermodynamic model for the lump ore, acid pellet, self-fluxed pellets and sinter, respectively. Since multi-component and multi-phase systems hardly form pure compounds, the oxide phases were overall expressed by its mineralogical form. Thus, Al-Hematite was majorly composed of Fe_2O_3 in solid solution with Al_2O_3 up to 1%. This phase is termed Corundum in the FactSage FToxid database but was represented as Al-Hematite to facilitate comprehension. The Spinel represents Fe_3O_4 with little amounts of Al and Mg, having a general formula AB_2O_4 where A = Fe^{2+}, Mg e B = Fe^{3+}, Al. The phase identified as MeO (Monoxide), describes a solid solution between Fe_2O_3, CaO, MgO and Al_2O_3, having FeO as its primary component. The $2CaO.SiO_2$ (C_2S) sum up both α and β phases, dissolving limited amounts of Mg_2SiO_4 and Fe_2SiO_4. The Calcium Ferrites denote the group of compounds with similar structure, such as CAF_3, CAF_1 and C_2AF, where C, A and F are

CaO, Al_2O_3 and FeO_x, respectively. Finally, Melilite, Olivine and Wollastonite are the compounds with general formula $Ca_2(Fe, Al, Si, Mg)_3O_7$, $(Ca, Fe, Mg)_2SiO_4$, $CaSiO_3$. It is important to mention that Olivine is a complex group that contains several different species. In this work, Calcio-Olivine (Ca_2SiO_4), Fayalite (Fe_2SiO_4) and Kirschsteinite ($CaFeSiO_4$) were the main species obtained for the samples simulated. In Figure 3.6 all Olivine species were identified in the same color as a reminder of its group of origin.

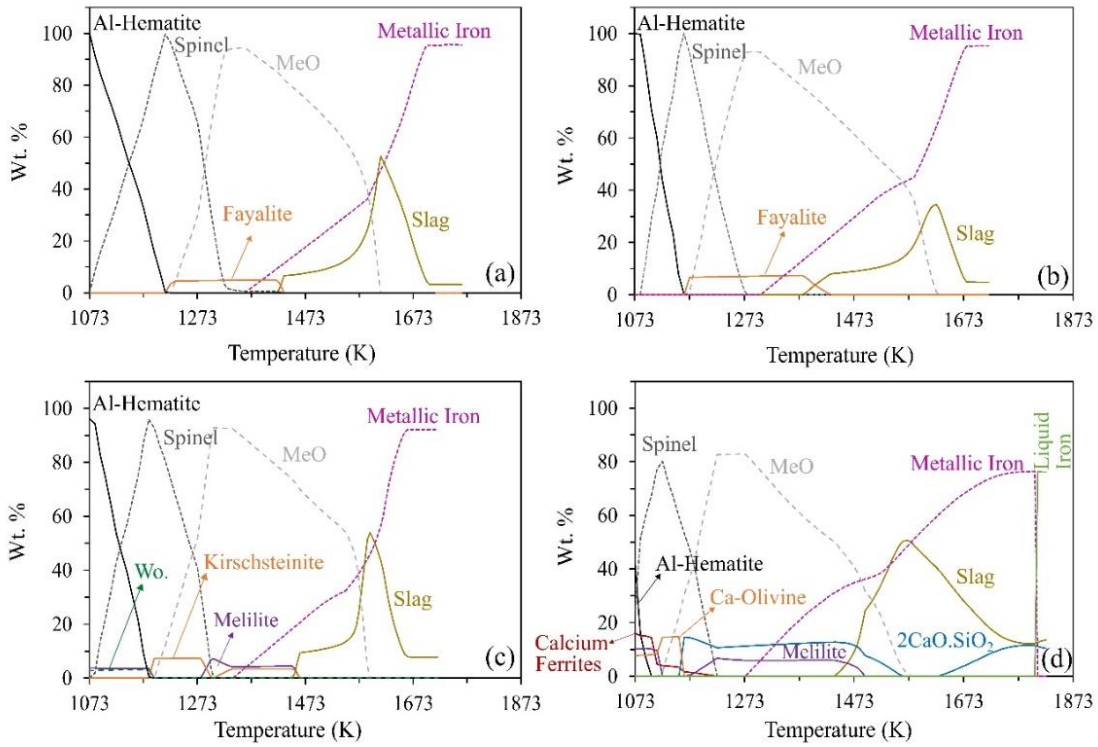

Figure 3.6. Detailed solid oxide phases composition obtained from the thermodynamic model for the lump ore (a), acid pellet (b), self-fluxed pellets (c) and sinter (d). Wo. = Wollastonite, Ca-Olivine = Calcio-Olivine

First of all, Al-Hematite (Fe_2O_3 rich for all materials), was the major starting iron oxide phase for the materials being simulated. Additionally, self-fluxed pellets (Figure 3.6 – c) showed Melilite ($Ca_2(Fe, Al, Si, Mg)_3O_7$) and Wollastonite ($CaSiO_3$) in equilibrium with Al-Hematite. For the sinter, Calcium Ferrites, Calcio-olivine (Ca_2SiO_4) and Melilite were also significant (Figure 3.6 – d). As temperature and hence reduction degree increased, equilibrium favored Al-Hematite reduction with the formation of Spinel (Fe_3O_4 rich for all materials). Concurrent, the Calcium Ferrites in sinter were also reduced and the

Melilite was assimilated by the Calcio-olivine. In comparison, Melilite and Wollastonite, initially in equilibrium in the self-fluxed pellets, combined to form Kirschsteinite ($CaFeSiO_4$).

For all materials, Spinel started to be reduced just after Al-Hematite complete reduction, leading to the formation of MeO (solid solution rich in FeO). For the lump ore and acid pellets, Fayalite (Fe_2SiO_4) was the main phase in equilibrium with MeO, which afterward participated in the formation of slag. For higher basicity materials such as self-fluxed pellets (Basicity of 1.15, Table 3.1), part of the Kirschsteinite previously formed decomposed to Melilite, having both phases in equilibrium with MeO up to slag formation. Also, in the sinter (Basicity of 2.07), Calcio-Olivine turned into C_2S, which after contributed to form Melilite. For this sample, slag was first formed by Melilite and MeO, and after by C_2S at slightly higher temperatures.

The overall evolution of the solid phases obtained by the model qualitatively agrees with the expected behavior of the different iron-bearing materials throughout reduction, softening and melting[5,6,26-28]. That is, before slag is formed, metallic iron and MeO are in accordance with the expected structure comprised of a metallic shell and an oxidic core, formed due to reduction following the shrinking core model. More specifically, although not entirely comparable due to some differences in chemical composition, Hotta and Yamaoka[28] reported acid and self-fluxed pellets (basicity = 0.05 and 1.54 respectively) reduced up to 1373K. The authors used X-ray diffraction to identify metallic iron, FeO, Fayalite and Hercynite ($FeO.Al_2O_3$) for the acid pellet and metallic iron, Magnesiowüstite (Fe,Mg)O and $CaFeSiO_4$ for the self-fluxed pellets. Those results are in good agreement with the phases obtained by the model for acid and self-fluxed pellets (Figure 3.6-b,c). Hercynite ($FeO.Al_2O_3$) was probably not found in the model due to the low Al_2O_3 content in the acid pellet (0.89 %) in comparison to Hotta and Yamaoka[28] pellet (2.94 %). For the Magnesiowüstite, more than 80% of the MgO initially contained in self-fluxed pellets were found to be in solution with FeO (MeO).

Furthermore, Hayashi *et al.*[8] reported the solid composition, obtained from X-ray diffraction, for a sinter (basicity = 2.19) reduced up to 1173, 1273, 1373 and 1473K using

experimental conditions similar to Nishimura *et al.*[16]. The authors found Fe_3O_4, FeO and C_2S in the sinter at 1173K. From that temperature up to 1273 and 1373K, C_2S remained present, while Fe_3O_4 was completely reduced and metallic iron was formed. At 1473K, the same phases were observed with the addition of $2CaO.Al_2O_3.SiO_2$. The phases reported by Hayashi *et al.*[8] agree with the calculated sinter oxide phases shown in Figure 3.6 – d. Other studies utilizing raw materials similar to those simulated and experimental conditions near those reported by Nishimura *et al.*[16] were not found. To further validate and adjust the model, and also better understand solid phases composition, structure and its influence on melt formation, softening and melting interrupted tests at specific temperatures are being planned for a range of iron-bearing materials.

In addition to the results showed in Figure 3.6, phase diagrams are of great interest to study slag formation. In the case of acid materials such as lump ore and acid pellets the proportion between Fayalite and MeO, as well as how Al and Mg are distributed in those phases may significantly alter the temperatures for melt formation. Thus, for those materials diagrams based on the $FeO\text{-}SiO_2$ system are necessary. For higher basicity materials such as self-fluxed pellets and sinter, Kirschsteinite, Melilite and C_2S were the main phases in equilibrium with Wüstite (MeO), generating a different equilibrium system for study ($FeO\text{-}SiO_2\text{-}CaO$). However, most ternary phase diagrams are projections of the *liquidus* surface instead of *solidus*, which may not be adequate to study softening and melting. Once *solidus* surfaces are hardly available in the literature[26,29], its derivation from *liquidus* projections or calculation using thermodynamic software may be of interest.

Concerning slag formation, Figure 3.7 (a-d) shows the detailed slag composition for the lump ore, acid pellets, self-fluxed pellets and sinter, respectively, as a function of equilibrium temperatures. It can be seen that slag was formed having FeO as its major component, present at 36.4% in self-fluxed pellets up to 63.2% in the lump ore. Moreover, after formation, the FeO in the slags increased with temperature reaching concentrations of roughly 80% for the lump ore and both pellets. Sinter was an exception, showing approximately constant FeO concentrations around 50%. Additionally, Fe_2O_3 appeared in the slags having a behavior similar to that of FeO. The Fe_2O_3 in the slag occurs due to

slag melting in equilibrium with metallic iron, with iron mostly in the divalent state, but some trivalent iron is also present. For that reason, some amount of Fe_2O_3 will be obtained at equilibrium[30]. The amount of Fe_2O_3 in equilibrium with FeO will depend on the concentration of SiO_2 and CaO in the slag. The former is considered to stabilize the divalent iron oxide, while the latter stabilizes the trivalent iron oxide[30]. The concentration of SiO_2, CaO, MgO and Al_2O_3 in the slags were different among the materials simulated due to contrasting differences in its initial chemical compositions.

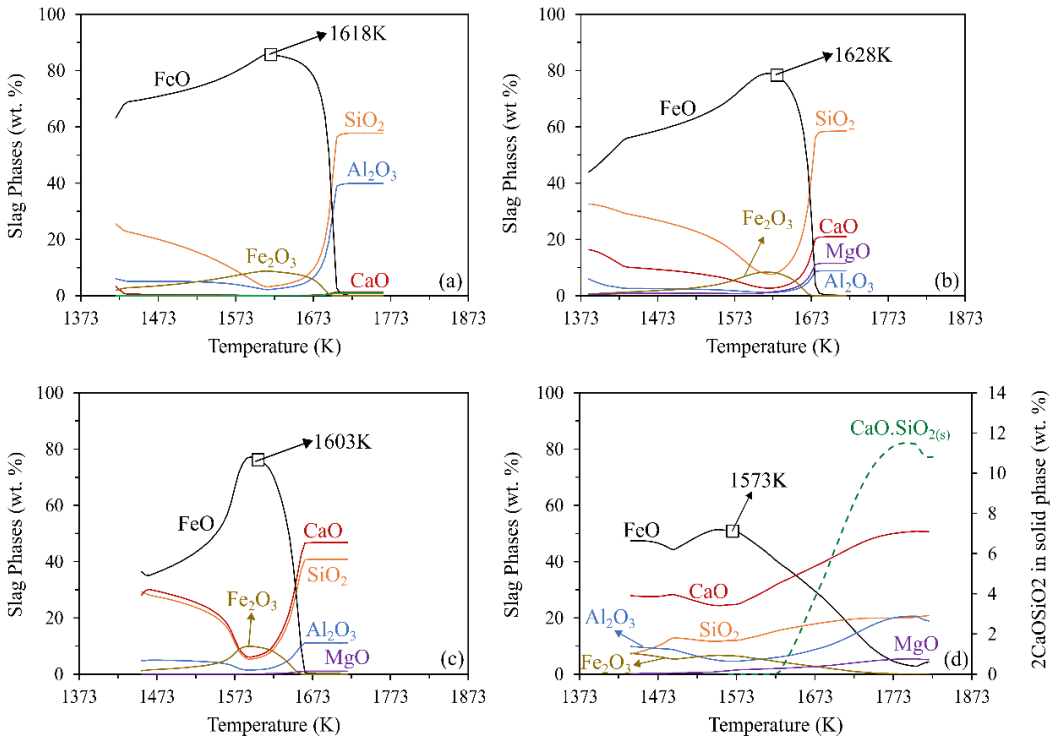

Figure 3.7. Detailed slag composition obtained from the thermodynamic model for the lump ore (a), acid pellet (b), self-fluxed pellets (c) and sinter (d). Highlighted temperatures identify the temperature where FeO reduction started

Furthermore, after FeO and Fe_2O_3 reached maximum concentration in the slags, melting reduction (temperatures indicated in Figure 3.7) started even thought carbon had been present in the simulations quite before (temperatures in Figures 3.3 and 3.4). It was not clear which phase containing FeO was preferentially reduced while the solid solution (MeO) and the ferrous slag coexisted. However, after MeO was totally reduced, the FeO content in the slag started to dimish, indicating its reduction. From the slope of the FeO curves in Figure 3.7, it can be seen that reduction was slower for the sinter. The latter can

occur due to C_2S precipitation as a result of the reduction of the FeO in the slag, which was observed around 1623K. According to Nishimura *et al.*[16] and Shigaki *et al.*[25], C_2S precipitation impede further contact between coke and slag, thus suppressing melting reduction.

3.4.3. Calculated Slag Mass Fraction vs. S&M Experimental Data

The transition from gangue to slag is of major importance for S&M of iron-bearing materials. According to Bakker T.[26], softening and consequently the deformation of reduced materials is triggered due to the formation of slag, which causes a drastic change in microstructure. The slag within the particles increases in volume as temperature rises, until exudation takes place and the slag flows out of particles' core to fill the voids of the bed. The latter sharply influences material permeability leading to an increase in the pressure drop across the bed.

Figure 3.8 (a-d) compares the calculated slag mass fraction profiles for each iron-bearing material with its respective experimental S&M results reported by Nishimura *et al.*[16]. The slag mass fraction was calculated as the ratio between the mass of liquid slag in relation to the total mass of material at each temperature. First of all, Figure 3.8 shows that the contraction profiles of all materials are relatively similar, presenting two distinct rates of contraction, although the temperature where contraction starts and its slope changed depend on the raw material. Regarding pressure drop, acid pellet showed the highest levels of pressure, followed by the sinter, self-fluxed pellets and lump ore, respectively (Figure 3.8 a-d). Additionally, the temperatures where pressure drop started to increase, reached its maximum and then returned to low levels were different for each sample.

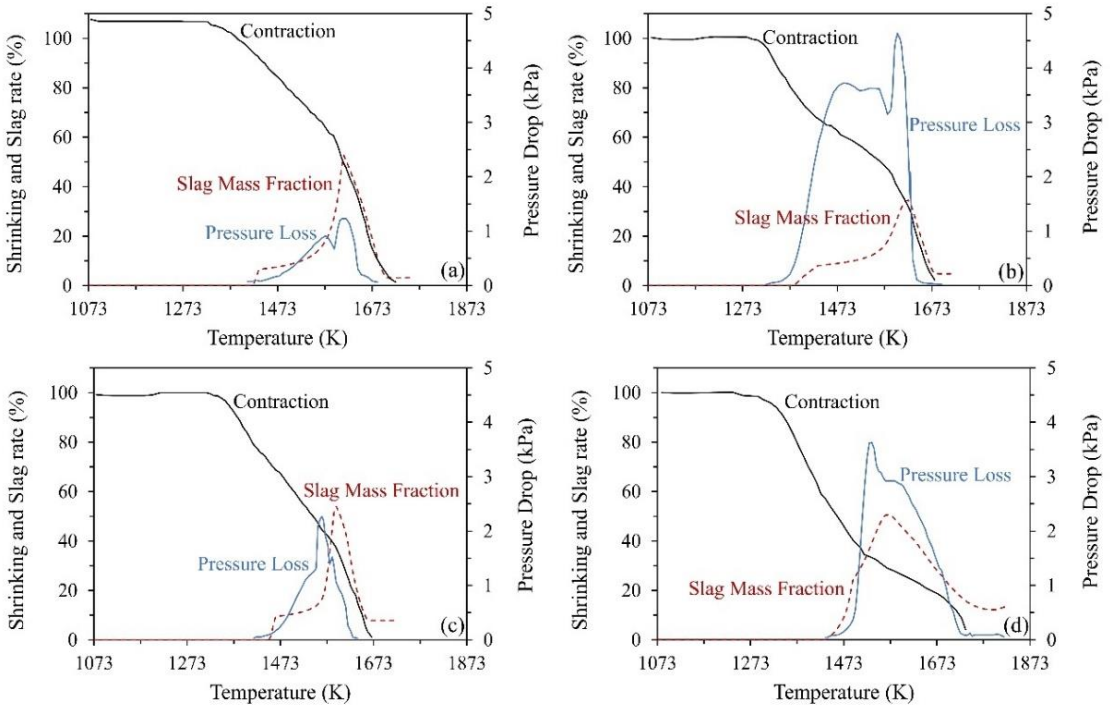

Figure 3.8. Comparison between experimental contraction and pressure loss, and calculated slag mass fraction for (a) lump ore, (b) acid pellet, (c) self-fluxed pellet and (d) sinter

It can be seen that the profiles of slag mass fraction were quite similar to those of pressure drop. To better compare experimental and calculated data, Table 3.2 lists some important parameters extracted from the contraction, pressure drop and slag mass fraction profiles. Experimentally, the following parameters were used: temperature of 10% sample contraction ($T_{C10\%}$), temperature of pressure drop increase above 2kPa (T_{S2}), temperature of maximum pressure drop (T_{Pmax}), temperature when pressure drop return to 2kPa (T_{E2}). The temperatures T_{S2} and T_{E2} correspond to the beginning and end of the cohesive zone while the difference between them represents the thickness of the cohesive zone. Additionally, the temperature of dripping start (T_D) was obtained directly from Nishimura et al.[16] and represents the moment where the liquid materials (iron and slag) start to drip from the bed of iron-bearing material and coke. Those experimental parameters were used to compare with the data from the slag profiles, temperature of slag formation (T_{SForm}), temperature of maximum slag amount ($T_{Slagmax}$), temperature of final slag (obtained when slag amount became stable after its maximum, $T_{SlagFinal}$) and the amount of slag at T_{S2} ($Slag_{\%TS2}$) were selected.

Table 3.2. Parameters taken from experimental S&M data showed in Figure 3.8 and calculated slag mass fraction for the iron-bearing materials simulated.

Parameters from S&M Experiments				
	Lump Ore	Acid Pellet	Self-fluxed Pellet	Sinter
$T_{C10\%}$ (K)	1406	1341	1383	1348
T_{S2} (K)	1477	1365	1462	1480
T_{Pmax} (K)	1610	1599	1562	1533
T_{E2} (K)	1639	1616	1595	1721
T_{D} (K)	1652	1615	1593	1724
Parameters from Calculated Slag				
	Lump Ore	Acid Pellet	Self-fluxed Pellet	Sinter
$T_{SlagForm}$ (K)	1418	1383	1453	1438
$T_{Slagmax}$ (K)	1613	1623	1593	1568
$T_{SlagFinal}$ (K)	1703	1678	1663	1753
$Slag_{\%TS2}$ (wt. %)	7.7	0	9.5	14.7

As already mentioned, material deformation is triggered by liquid slag formation. Thus, the temperature $T_{C10\%}$ should be close to that of $T_{SlagForm}$. At Table 3.2 it can be seen that those temperatures were very similar for the lump ore. However, they became increasingly more distant for the acid pellets, self-fluxed pellets and the sinter, respectively. According to Bakker *et al.*[26], more heterogeneous materials usually form slag at lower temperatures in comparison to a homogeneous condition[26]. Similar to that, Barnaba T.[31] investigated the influence of the size of lime added at sinter and reported that the finer the lime the higher temperature of slag formation.

It is accepted that finer materials are more homogeneous and thus usually closer to equilibrium. In this sense, the more types of ores used and higher amounts of fluxes added into a given iron-bearing material, the higher its degree of heterogeneity. Additionally, pellets induration and the sintering process add some heterogeneity in the material as well. For the samples simulated, the following order of heterogeneity can be established based on each material type: lump ore, acid pellet, self-fluxed pellet and sinter, from more homogeneous to more heterogeneous. The latter agrees very well with the increasing difference between $T_{C10\%}$ and $T_{SlagForm}$ from the lump ore to the sinter.

Comparatively to that, temperature T_{S2}, which is related to when liquid slag exudes to the bed, was more similar to $T_{SlagForm}$ as materials heterogeneity increased. It seems that as slag is formed and evolves the system strives towards establishing equilibrium. Thus, after a sufficient development of liquid, experimental and calculated parameters tend to

approach even at more heterogeneous conditions. Moreover, the amount of slag calculated at the moment of pressure drop increase ($Slag_{\%TS2}$) was similar for all materials, except for the acid pellet.

Furthermore, temperatures of maximum pressure drop (T_{Pmax}) and maximum slag formation ($T_{Slagmax}$) were quite similar for all materials simulated. According to Liu *et al.*[18], when T_{Pmax} is reached during S&M experiments primary-slag is totally produced. At this moment, experimental materials may achieve conditions near equilibrium. Lastly, the temperature where the pressure drop returns to initial levels (T_{E2}) and the dripping start temperature (TD) were quite similar, both greatly different from those of final slag ($T_{SlagFinal}$). Such differences are probably associated with parameters such as slag viscosity and surface tensions, which may play a significant role in the dripping stage[9].

3.5. Conclusion

The current status of a thermodynamic model incorporating parameters to partly consider reduction kinetics was described in details and the first results presented were compared with literature data. Detailed results regarding different iron-bearing materials reduction and composition (solids and liquids) were showed and compared to experimental data of S&M experiments. The major findings are as follows:

1. The calculation method suggested to the present thermodynamic model achieved good agreement between experimental and calculated data by the use of splitters to partly consider reduction kinetics from empirical parameters;
2. The composition for the materials solid phases was obtained as a function of temperature, having a good agreement with the available literature data for acid pellets, self-fluxed pellets and the sinter in qualitative terms;

3. Fayalite was found the be the major phase in equilibrium with MeO (FeO rich solid solution) for materials with low basicity such as lump ore and acid pellet. For the self-fluxed pellets Kirschsteinite, Melilite and MeO were the precursors of melt. For the

sinter, Melilite and MeO firstly participated in slag formation, which after had the contribution of C_2S;

4. The slag of all iron-bearing materials was found to be very rich in FeO, which was reduced very fast when melting reduction took place. For the sinter, the precipitation of C_2S was observed near after melting reduction started, which was associated with the lower rate of melting reduction of this material;

5. Experimental pressure drop and calculated slag rate profiles were similar for all materials. However, the level of heterogeneity of different iron-bearing materials may significantly alter which calculated and experimental parameters can be interpreted. More homogeneous materials like lump ore showed good results in comparison to slag formation, while more heterogeneous materials like sinter presented good results regarding pressure drop increase. All samples simulated had a good agreement between the temperature of maximum pressure drop and maximum slag formation.

Acknowledgments

The authors express gratitude to CAPES-PROEX, CNPq and FAPEMIG for stimulating and supporting research.

3.6. References

1. N.J. Busby, T.A.T. Fray and D.C. Goldring: *Ironmaking Steelmaking*, 1994, vol. 21, pp. 229-236.
2. N. Nakamura, Y. Togino, T. Tateoka: *Ironmaking Steelmaking*, 1978, vol. 5, pp; 1-17.
3. W. Yang, Z. Zhou, D. Pinson and A. Yu: *Metall. Trans. B*, 2015, vol. 46B, pp. 977-992.
4. X.F. Dong, A.B. Yu, S.J. Chew and P. Zulli: *Metall. Trans. B*, 2010, vol. 41B, pp. 330-349.

5. J. Sterneland and A.K. Lahiri: *Ironmaking Steelmaking*, 1999, vol. 26, pp. 339-348.

6. P.F. Nogueira and R.J. Fruehan: *Metall. Trans. B*, 2004, vol. 35, pp. 829-838.

7. Y. Omori: *Blast Furnace Phenomena and Modelling*, Elsevier, London, UK, 1987.

8. M. Hayashi, K. Suzuki, Y. Maeda and T. Watanabe: *ISIJ Int*, 2015, vol. 55, pp. 1223-1231.

9. P. Kaushik, R.J. Fruehan: *Ironmaking Steelmaking*, 2006, vol. 33, pp. 507-519.

10. X. Liu, T. Honeyands, G. Evans, P. Zulli and D. O'Dea: *Ironmaking Steelmaking*, 2018.

11. Kemppainen, K. Ohno, M. Iljana, O. Mattila, T. Paananen, E. Heikkinen, T. Maeda, K. Kunitomo and T. Fabritius: *ISIJ Int*, 2015, vol. 55, pp. 2039-2046.

12. W.T. Guo, Q.G. Xue, Y.L. Liu, X.F. She and J.S. Wang: *Ironmaking Steelmaking*, 2016, vol. 43, pp.22-30.

13. X. Liu, S. Wu, W. Huang, K. Zhang, K. Du: *ISIJ Int*, 2014, vol. 54, pp. 2089-2096.

14. P. Kaushik and R.J. Fruehan: *Ironmaking Steelmaking*, 2006, vol. 33, pp. 520-528.

15. P. Kaushik and R.J. Fruehan: *Ironmaking Steelmaking*, 2007, vol. 34, pp. 10-22.

16. T. Nishimura, K. Higuchi, M. Naito and K. Kunitomo: *ISIJ Int*, 2011, vol. 51, pp. 1316-1321.

17. K. Ichikawa, J. Ishii, S. Watakabe and M. Sato: *ISIJ Int*, 2015, vol. 55, pp. 544-551.

18. S. L. Wu, B. Su, X. L. Liu and M. Y. Kou: Ironmaking Steelmaking, 2018, vol. 45, pp. 50-57.

19. P. Koukkari and R. Pajarre: *CALPHAD: Comput. Coupling Phase Diagrams Thermochem.*, 2006, vol. 30, 18-26.

20. K. Hack: *The SGTE Casebook Thermodynamics at Work*, Woodhead Publishing Limited, Cambridge, England, 2008.

21. S. Petersen, K. Hack, P. Monheim and U. Pickartz: *Int. J. Mat. Res.*, 2007, vol, 98, pp. 946-953.

22. J.H. Strassburger: *Blast Furnace Theory and Practice*, Gordon and Breach, New York, 1969.

23. C.W. Bale, E. Bélisle, P. Chartrand, S.A. Decterov, G. Eriksson, K. Hack, I.-H. Jung, Y.-B. Kang, J. Melançon, A.D. Pelton, C. Robelin and S. Petersen: *CALPHAD: Comput. Coupling Phase Diagrams Thermochem.*, 2009, vol. 33, pp. 295-311.

24. T. Bakker and R.H. Heerema: *Ironmaking Conf. Proc.*, 1998, pp. 1597-1608.

25. I. Shigaki, S. Shirouchi, K. Tokutake and N. Hasegawa: *ISIJ Int*, 1990, vol. 30, pp. 199-207.

26. T. Bakker: Dissertation, *Softening in the Blast Furnace Process: Local Melt Formation as the Trigger for Softening of Ironbearing Burden Materials*, Delft University of Technology, Netherlands, 1999, pp. 272.

27. K. Higuchi, M. Naito, M. Nakano and Y. Takamoto: *ISIJ Int*, 2004, vol. 44, pp. 2057-2066.

28. H. Hotta and Y. YAMAOKA: *ISIJ Meeting*, 1984, vol. 107, pp. 294-301.

29. H.-C. Chuang, W.-S. Hwang and S.-H. Liu: Mater. Trans., 2009, vol. 50, pp. 1448-1456.

30. T. Rosenqvist: *Principles of Extractive Metallurgy*, Tapir Academic Press, Trondheim, 2004.

31. P. Barnaba: Ironmaking Steelmaking, 1985, vol. 12, pp. 53-63.

Capítulo 4. Considerações Finais

Nesse trabalho, o comportamento de amolecimento e fusão de diferentes tipos de cargas ferrosas foi avaliado através de uma abordagem experimental e de um modelo termodinâmico. O primeiro artigo (Capitulo 2) tratou da evolução da microestrutura de um minério granulado, uma pelota ácida e um sínter, durante o avanço do processo de amolecimento e fusão. Já o segundo artigo (Capitulo 3) abordou em detalhes os métodos utilizados para a construção de um modelo termodinâmico utilizando o software FactSage.

No que diz respeito ao primeiro artigo, três cargas ferrosas utilizadas em altos-fornos tiveram suas propriedades em alta temperatura avaliadas através de testes de amolecimento e fusão, executados no equipamento existente no Laboratório de Processos Siderúrgicos (LPS) da UFMG. Além disso, testes interrompidos foram realizados para verificar os fenômenos e microestruturas associados aos diferentes estágios de amolecimento e fusão de cada amostra.

À medida que o processo de amolecimento e fusão avançou, da temperatura $T_{10\%}$ para $T_{50\%}$, todas as amostras apresentaram uma estrutura bem definida e composta por uma matriz de escória e glóbulos de wüstita (Figura 2.11). O crescimento das estruturas associadas à formação de líquido não é comumente mencionado na literatura, mas é importante para demonstrar o efeito da temperatura sobre a microestrutura associada ao amolecimento e fusão. Além disso, a diferença no tamanho dos glóbulos de wüstita entre as amostras é nítida, os quais foram maiores para o minério, seguido do sínter e da pelota (o inverso é valido para a quantidade de líquido). O tamanho dos glóbulos de wüstita parece estar relacionado à quantidade de líquido formado, a qual também afeta a espessura da escória que preenche os contornos de grão. Esses resultados podem ser pertinentes à taxa de contração das cargas ferrosas. Cada carga apresentou uma taxa de contração distinta, mas constante ao longo do intervalo de temperatura de $T_{10\%}$ até $T_{50\%}$ (Figura 2.4). A pelota ácida apresentou a maior taxa de contração (2,73 %/K), seguida pelo sínter (2,05 %/K) e pelo minério (1,1 %/K).

Os valores das taxas de contração estão de acordo com a análise qualitativa da quantidade de líquido de cada material, sendo que quanto maior a fração de líquido formada, maior a taxa de contração da carga ferrosa. Esse resultado vai ao encontro do estudo de Bakker et al.[1], onde para cilindros composto por misturas de wüstita e faialita, a taxa de contração foi proporcional à quantidade de líquido. No entanto, os autores relatam que, na presença de casca metálica, a taxa de deformação é controlada somente pela espessura da casca e irá depender do nível de pré-redução da carga. Nesse sentido, o grau de redução das amostras testadas imediatamente antes do início de contração (temperatura onde o deslocamento do leito teve início) foi de 23, 36 e 53%, para o minério, a pelota e o sínter, respectivamente. Considerando que quanto maior o grau de redução, mais espessa a casca metálica, e consequentemente menores as taxas de deformação, os resultados de grau de redução são inversamente proporcionais ao observado para as taxas. Isso indica que, apesar da formação da casca metálica, a estrutura do núcleo ainda deve influenciar o processo de deformação.

Concomitantemente à contração dos leitos de amostra, entre $T_{10\%}$ e $T_{50\%}$, ocorreu o fenômeno de retardo de redução (Figura 2.5). Com exceção do minério, sabendo que na temperatura $T_{10\%}$ líquido já havia sido formado para desencadear a contração, existe um intervalo de temperatura no início do estágio de amolecimento onde o retardo de redução não ocorre. É possível que haja um limite de fração líquida acima do qual os fenômenos de migração de escória, e consequentemente retardo de redução, iniciem. A Figura 4.2 apresenta um esquema geral de como acredita-se que o processo de retardo de redução ocorra. Inicialmente, a redução da carga ferrosa gera um acréscimo de porosidade aberta e formação de casca metálica. Com o aquecimento e andamento da redução, a espessura da casca metálica aumenta e a contração tem início. Por fim, a escória líquida formada no interior das partículas migra para a periferia e preenche os poros da casca metálica (diminuição brusca de porosidade aberta, Figura 2.9), causando um acentuado retardo de redução.

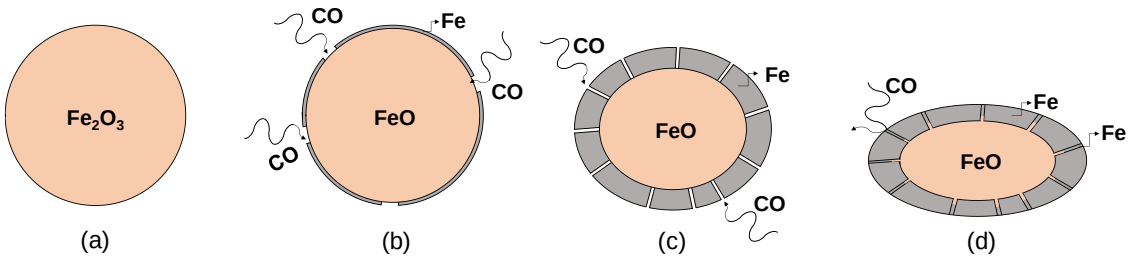

Figura 4.1. Evolução da estrutura das partículas durante o retardo de redução, onde: (a) condição inicial, (b) redução com formação de casca metálica, (c) contração da partícula e espessamento da casca metálica pela continuidade da redução e (d) migração de escória e preenchimento dos poros da casca metálica em contração elevada.

Em comparação com o primeiro artigo, o modelo termodinâmico desenvolvido (artigo B) determinou a evolução das fases sólidas e da fase líquida continuamente em função da temperatura. Através do modelo também foi possível determinar as temperaturas de formação e o perfil da quantidade de líquido durante a redução, amolecimento e fusão das cargas ferrosas (Figura 3.6). Com exceção do sínter, as amostras de minério e pelotas investigadas pelo modelo obtiveram perfis de fase líquida similares. Após a formação inicial, a quantidade de líquido atingiu um leve patamar, o qual se manteve relativamente estável até aumentar abruptamente. Esse patamar de líquido inicial pode ter relação com os fenômenos de deformação e retardo de redução comentados. A formação de um patamar pode explicar porque a taxa de deformação de cada material permanece praticamente constante à medida que a temperatura aumenta (Figura 3.8). A taxa de contração só se alterou significativamente na transição entre os estágios de amolecimento e de exsudação, e pode estar relacionada ao abrupto aumento da quantidade de líquido. Ademais, o patamar de líquido inicial também pode estar relacionado com a inércia do fenômeno de migração de escória, o qual parece ocorrer somente a partir de uma certa quantidade de líquido.

No que diz respeito à relação entre os parâmetros experimentais de amolecimento e fusão e os resultados do modelo, as temperaturas de formação de líquido simuladas foram próximas às temperaturas de início de amolecimento ($T_{C10\%}$). Para essas temperaturas, o nível de proximidade entre os parâmetros experimental e simulado foi dependente da heterogeneidade de cada material. Para tanto, baseado na quantidade de ganga e no método de fabricação da carga ferrosa, o minério granulado foi considerado como o

material mais homogêneo, enquanto o sínter foi o mais heterogêneo. Quanto mais homogêneo o material, mais próximos os parâmetros de formação de líquido experimental e simulado. Além disso, com o aumento da temperatura, e consequentemente, da quantidade de líquido, os resultados experimentais e simulados ficaram mais próximos. Isso mostra que para maiores quantidades de líquido, a situação experimental aproxima-se da termodinâmica. Esse resultado mostra que o modelo desenvolvido consegue simular a evolução das fases durante o amolecimento e fusão. Em especial, os perfis de líquido calculados foram bastante similares às curvas de perdas de pressão experimentais.

O modelo termodinâmico atual apresentou uma flexibilidade interessante quanto as condições de entrada (composição química, atmosfera e pressão). Uma vez que se obtenham o perfil térmico, gasoso e grau de redução, é possível modificar o modelo para simular outros equipamentos de amolecimento e fusão. Em contrapartida, a partir de um material conhecido e para uma condição de atmosfera específica, pode-se avaliar como diferentes atmosferas redutoras e alterações de composição química podem afetar o comportamento de redução. Os *splitters* para o controle das reações permitem também que diferentes taxas de aquecimento possam ser avaliadas.

Para avançar com o desenvolvimento do modelo apresentado além de seu estado atual, os resultados obtidos a partir do artigo A serão fundamentais. Os dados de grau e taxa de redução, bem como os de consumo de carbono, irão contribuir para aprimorar o cálculo dos *splitters* gasosos e de carbono para o ajuste cinético da redução. Além disso, a comparação dos perfis dos *splitters* dessas amostras com os obtidos no artigo B, utilizando os dados da literatura, possibilitará verificar diferenças e similaridades entre diversos tipos de amostras. A caracterização das fases, porosidade e microestrutura realizada para os produtos dos testes interrompidos irá auxiliar na validação da composição das fases sólidas e fase líquida calculadas pelo modelo, bem como no seu ajuste e futuro desenvolvimento.

4.1. Referencias

1. T. Bakker and R.H. Heerema: *Ironmaking Conf. Proc.*, 1998, pp. 1597-1608.

Capítulo 5. Contribuições Originais ao Conhecimento

As principais contribuições do presente trabalho para o avanço do conhecimento na área de comportamento em alta temperatura de cargas ferrosas para alto-forno foram:

1. A evolução da microestrutura de três tipos de cargas ferrosas foi investigada frente ao processo de amolecimento e fusão por análises de densidade (porosidade), microscopia óptica e microscopia eletrônica de varredura. Pelos resultados obtidos, os diferentes comportamentos de redução, amolecimento e fusão foram obtidos, contribuindo com a literatura para a compreensão dos fenômenos envolvidos;

2. Criou-se um modelo termodinâmico combinado com o uso de operadores baseados em dados experimentais para, de maneira simples, modelar a redução de cargas ferrosas em alta temperatura, abordando tanto os fenômenos de retardo de redução quanto redução em estado líquido. Essa metodologia contribui para a maior aplicação e desenvolvimento de modelos baseados em softwares termodinâmicos onde a cinética precisa ser considerada;

3. Através do modelo desenvolvido, a evolução das fases sólidas e da fase líquida foi obtida em comparação com os parâmetros dos experimentos de amolecimento e fusão. Isso permitiu trazer novas relações entre as fases, especialmente a fase líquida, com os fenômenos conhecidos.

Capítulo 6. Contribuições para a Literatura

6.1. Publicações Geradas a Partir da Presente Tese

6.1.1. Artigos Publicados em Periódicos

Flores, I.V., Silva, A.L., Heck, N.C., Bagatini, M.C., A Thermodynamic Model Towards the Comprehension of Ferrous Burden Softening and Melting Using FactSage Macro Processing. Metallurgical and Materials Transactions B, 2019, In Press. Qualis A1.

6.1.2. Artigos Submetidos em Periódicos

Flores, I.V., Matos, O., Silva, A.L., Bagatini M.C., Microstructure and Porosity Evolution During the Reduction, Softening and Melting of Iron-bearing Materials. Metallurgical and Materials Transactions B. Qualis A1.

6.1.3. Artigos Publicados em Anais de Congressos

Assis, O.H.M., Flores, I.V., Bagatini, M.C., Caracterização do Retardo de Redução para Sínter e Pelota Durante o Amolecimento e Fusão. In: 49° Seminário de Redução de Minérios e Matérias-primas, 2019, São Paulo.

Flores, I.V., Silva, A. L., Heck, N. C., Bagatini, M. C. Amolecimento e fusão de cargas ferrosas: avaliação de um modelo termodinâmico. In: 48° Seminário de Redução de Minérios e Matérias-primas, 2018, São Paulo. 48° Seminário de Redução de Minérios e Matérias-primas, 2018. v. 48. p. 317-329.

Flores, I.V., Silva, A. L., Heck, N. C., Bagatini, M. C. Towards the comprehension of ferrous burden softening and melting phenomena in blast furnace: development of a thermodynamic approach. In: 8th International Congress on Science and Technology of Ironmaking, 2018, Viena. 8th International Congress on Science and Technology of Ironmaking, 2018. v. 8.

Almeida, L.B., Flores, I.V., Bagatini, M.C., Atualização e validação de um equipamento de amolecimento e fusão de cargas ferríferas. In: 47º Seminário de Redução de Minérios e Matérias-Primas, 2017, São Paulo. Anais dos Seminários de Redução, Minério de Ferro e Aglomeração. São Paulo: Editora Blucher, 2017. v. 47. p. 375.

6.2. Outras Publicações no Decorrer da Formação Acadêmica

6.2.1. Publicações em Periódicos

Malaquias, B., Flores, I.V., Bagatini, M.C., Effect of High Petroleum Coke Additions on Metallurgical Coke Quality and Optical Texture. REM – International Engineering Journal. 2019. Submetido.

Flores, I.V.; Fraiz, F.; Lopes Junior, R. A.; Bagatini, M. C. Evaluation of spent pot lining (SPL) as an alternative carbonaceous material in ironmaking processes. Journal of Materials Research and Technology-JMR&T, v. 8, p. 33-40, 2019.

6.2.2. Publicações em Anais de Congressos

Oliveira, A.F.L., Lopes Jr., R.A., Flores, I.V., Bagatini, M.C., Adição de pellet feed na aglomeração a frio de minério de ferro para sinterização. In: 49° Seminário de Redução de Minério de Ferro e Matérias-Primas e 7° Simpósio Brasileiro de Aglomeração de Minério de Ferro, 2019, São Paulo.

Silva, R.T., Fernandes, T.A., Flores, I.V., Bagatini, M.C., Avaliação em alta temperatura de briquetes compostos por carepa e pó de balão. In: 18° ENEMET, 2018, São Paulo. ABM Proceedings, 2018. v. 18. p. 192.

Fraga, M. T.; Flores, B. D.; Flores, I. V.; Schander, L. G.; Silva, G. L. R.; Vilela, A. C. F.; Osório, E. Influência do tamanho de partícula sobre as propriedades termoplásticas de carvões coqueificáveis importados e brasileiro. In: 47º Seminário de Redução de Minérios

e Matérias-Primas, 2017, São Paulo. Anais dos Seminários de Redução, Minério de Ferro e Aglomeração. São Paulo: Editora Blucher, 2017. v. 47. p. 264

Oliveira, A.F.L.; Lopes, R. A.; Flores, I.V.; Bagatini, M.C. Efeito de finos de coque e do recobrimento em quase-partículas. In: 18° ENEMET, 2018, São Paulo. ABM Proceedings, 2018. v. 18. p. 169.

Capítulo 7. Sugestões para Trabalhos Futuros

Os seguintes temas são sugeridos como trabalhos futuros:

1. Averiguar o efeito da participação do gás hidrogênio sobre a redução, amolecimento e fusão de diferentes cargas ferrosas utilizando tanto a rota experimental pré-estabelecida, quanto o modelo desenvolvido;

2. Avaliar, a partir de experimentos e da aplicação do modelo para cargas individuais, o potencial do modelo termodinâmico para investigar o comportamento de amolecimento e fusão de cargas ferrosas mistas;

3. Validar e aprimorar o modelo termodinâmico desenvolvido quanto a evolução de fases solidas e líquida em função da temperatura utilizando novos estudos experimentais;

4. Investigar possíveis relações entre as propriedades físicas e químicas de cargas ferrosas, como porosidade e basicidade, com as funções *splitters* utilizadas para tratar as limitações cinéticas durante a redução, as quais possibilitariam novas abordagens para a criação e o aprimoramento de modelos;

5. Investigar a relação entre a taxa de contração com os fenômenos de migração de escória e retardo de redução através de ensaios de amolecimento e fusão com cargas mecânicas variadas e execução de testes interrompidos;

6. Quantificar por análise de imagem a área e volume percentuais das fases sólidas e líquida e da porosidade durante o processo de amolecimento e fusão, possibilitando determinar a fração de líquido, sua distribuição, o tamanho médio dos glóbulos de wüstita e a porosidade em função da temperatura.

APÊNDICE A - Determinação de Densidade Aparente e Real

A Figura A.1 apresenta em maiores detalhes a metodologia utilizada para a determinação das densidades (a) aparente e (b) real das amostras de amolecimento e fusão interrompidas. A Figura A.1-a mostra o aparato utilizado para determinar a densidade aparente e a porosidade aberta das amostras. Para tanto, foi utilizado o princípio de Arquimedes a partir das equações A.1 e A.2, onde W_1 é a massa de amostra obtida ao ar, W_2 é a massa de amostra submersa em água e W_3 é a massa da amostra ao ar após sua imersão em água. Nessa última, os poros abertos da amostra permanecem preenchidos com água, permitindo obter a massa de água que preenche os poros da amostra. Para a obtenção de W_3 a água na superfície das partículas foi seca com auxílio de papel toalha.

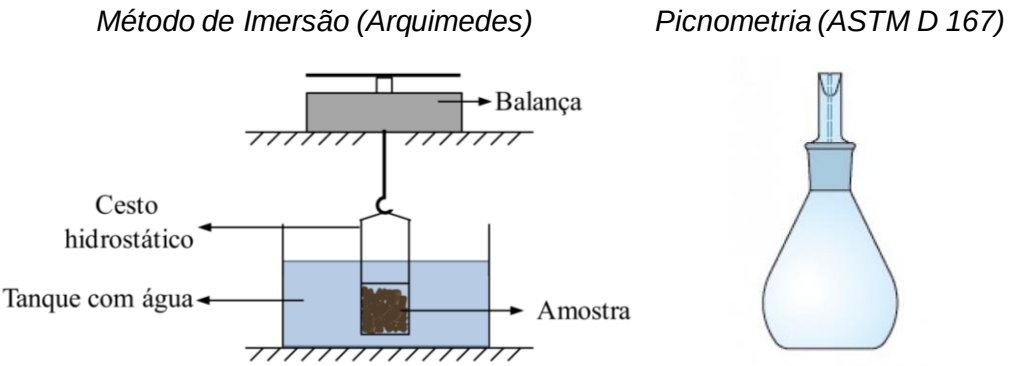

Figura A.1. Esquema das técnicas de imersão (a) e picnometria (b) utilizadas para a determinação da densidade aparente e real.

Já para a determinação das densidades reais, as amostras foram cominuídas abaixo de 0,044 mm e submetidas a testes de picnometria (Figura A.2). A densidade real é obtida pela Equação A.3, onde W_{P1} é a massa de amostra seca, W_{P2} é a massa do picnômetro, mais a massa da amostra seca mais a massa de água necessária para preencher o picnômetro e W_{P3} é a massa do picnômetro mais a massa de água para preenchê-lo.

$$\rho_{aparente} = \rho_{H_2O}\, x\, {}^{W_1}/_{W_3 - W_2} \quad \text{(A.1)}$$

$$Porosidade\ aberta\ (\%) = 100\, x\, {}^{(W_3 - W_1)}\Big/_{(W_3 - W_2)} \quad \text{(A.2)}$$

$$\rho_{real} = {}^{W_{P1}}/_{(W_{P1} - (W_{P2} - W_P))} \quad \text{(A.3)}$$

$$Porosidade\ Total\ (\%) = 100\, x\, \left(1 - {}^{\rho_{aparente}}/_{\rho_{real}}\right) \quad \text{(A.4)}$$

APÊNDICE B - Aspecto dos Leitos de Amostra Interrompidos

Figura B.1. Aspecto visual dos leitos de amostra obtidos a partir dos testes interrompidos para o minério granulado, pelota ácida e sínter metalúrgico.

APÊNDICE C – Conceitos Básicos da Concepção do Modelo Termodinâmico

O presente apêndice tem como objetivo apresentar de forma mais completa os conceitos empregados para a construção do modelo termodinâmico presente no Artigo B (pg. 42). Para a total compreensão do conteúdo aqui exibido, recomenda-se que a metodologia descrita no Artigo B também seja considerada. Também se recomenda a consulta ao livro "The SGTE Casebook Thermodynamics at Work" de Klaus Hack.

Para fundamentar os conceitos aplicados na construção do modelo termodinâmico, primeiro devemos definir o que são correntes. Durante a simulação termodinâmica em FactSage, diversas correntes são utilizadas como entrada ou são obtidas como saída (resultado) dos cálculos de equilíbrio. Um exemplo de uma corrente pode ser uma mistura de gases a ser utilizada como input para uma certa condição de equilíbrio. Além disso, os resultados obtidos de um cálculo de equilíbrio são divididos em diversas correntes, cada uma contendo uma fase/solução específico ou uma mistura desses.

Para a construção de um modelo capaz de simular processos dinâmicos, como os altos-fornos ou equipamentos de amolecimento e fusão, reatores de equilíbrio podem ser empregados para representar uma determinada condição/região do processo. A Figura C.1-a apresenta um desses reatores, onde para uma carga ferrosa composta majoritariamente por óxidos de ferro tem-se a definição da temperatura desejada e a introdução do gás redutor. Como produtos, os gases são eliminados, enquanto que as fases condensadas (sólidos e líquidos) são utilizadas nos reatores de equilíbrio subsequentes. A montagem de diversos desses reatores em série permite varrer o processo dinâmico que se tem interesse, como exemplificado na Figura C.1-b. De acordo com os estudos apresentados ao longo desse trabalho, o modelo desenvolvido teve como foco experimentos de amolecimento e fusão, os quais podem ser considerados como um reator de leito fixo, ou seja, os gases permeiam a amostra de baixo para cima, enquanto as fases condensadas permanecem no leito estacionário (Figura 2.1). O número de reatores de equilíbrio a ser utilizado irá depender do intervalo de temperatura a ser considerado e do incremento de temperatura entre os reatores. Além disso, o número de reatores de equilíbrio deve ser suficiente para varrer o intervalo de temperatura desejado em detalhe.

Usualmente, quanto maior o número de reatores de equilíbrio, melhor a resposta do modelo, no entanto o tempo de cálculo pode se tornar excessivo. A composição gasosa de entrada em cada reator de equilíbrio será determinada a partir das vazões de entrada no equipamento de amolecimento e fusão simulado e pelo incremento de temperatura definido.

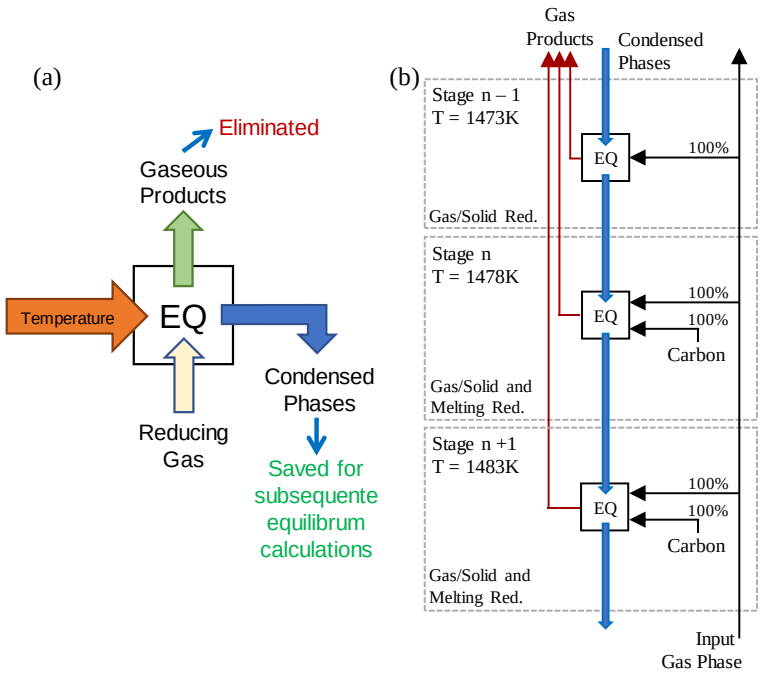

Figura C.1. (a) reator de equilíbrio individual e (b) combinação de reatores de equilíbrio em série para simular reator em contracorrente.

O modelo termodinâmico apresentado na Figura C.1-b não leva em consideração nenhum tipo de restrição cinética. Nele, todo o gás redutor e carbono existentes em cada reator de equilíbrio são utilizados para o cálculo de equilíbrio, usualmente superestimando o processo real. Para contornar esse problema, o uso de *splitters*, operadores matemáticos calculados com base em dados empíricos, pode ser realizado. Os *splitters* apresentam três funções principais: (1) determinar qual caminho uma corrente (uma mistura gasosa, por exemplo) irá seguir (fluir) de uma região de equilíbrio para uma região vizinha, (2) determinar a quantidade de uma corrente que irá reagir em uma região de equilíbrio e (3) dividir uma corrente composta por uma mistura de compostos em diversas correntes, separando os compostos inicialmente obtidos.

A Figura C.2 exemplifica o uso dos *splitters* para a separação de uma fase gasosa ao longo de uma sequência de equilíbrio em um reator em contracorrente. Nesse caso, as fases condensadas (fases sólidas e líquidas) são utilizadas como entrada para um cálculo de equilíbrio (extremidade esquerda da figura). O resultado obtido é introduzido em um *splitter* para realizar a separação entre as fases condensadas e a fase gasosa. Além disso, o *splitter* também determina o caminho da fase gasosa, possibilitando que o produto gasoso de uma reação (ΔH_2, por exemplo) seja utilizado como entrada para uma reação subsequente (ΔH_1). Similarmente, as fases condensadas são transferidas de uma condição de equilíbrio para outra subsequente.

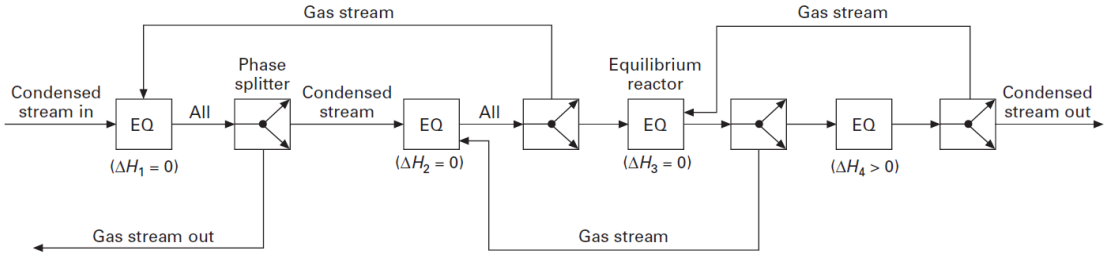

Figura C.2. Sequência de equilíbrio utilizando *splitters* para a separação da fase gasosa (K. Hack, 2008).

Em comparação, a Figura C.3 apresenta como os splitters podem ser empregados para determinar a quantidade de uma corrente, obtida a partir de um reator de equilíbrio, que será utilizada nos estágios subsequentes. Nesse caso, partindo do estágio de equilíbrio número 4, 80% do produto gasoso é direcionado para o estágio de equilíbrio 3. Ademais, dos 20% restantes, 25% é direcionado para o estágio de equilíbrio 1 e 75% para o estágio 2. Considerando um fluxo gasoso de baixo para cima em um reator em contracorrente, o produto gasoso de um estágio de equilíbrio com posição mais inferior no reator é utilizado como entrada para os estágios de equilíbrio localizados mais acima.

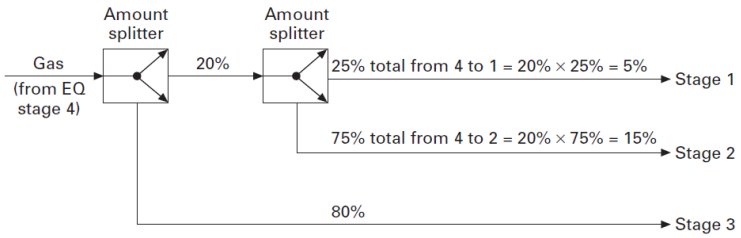

Figura C.3. Aplicação de *splitters* para determinar a quantidade de gás saindo de um estágio de equilíbrio para estágios vizinhos (K. Hack, 2008).

A partir dos *splitters*, o modelo construído na Figura C.1-b pode ser ajustado para considerar, em parte, restrições cinéticas. Similar ao apresentado na Figura C.3, os *splitters* podem ser utilizados para restringir a quantidade de gás disponível em cada reator de equilíbrio, limitando assim a redução dos óxidos de ferro. A Figura C.4 apresenta a transição do modelo sem *splitters* para a condição com o uso de splitters para considerar a cinética da redução.

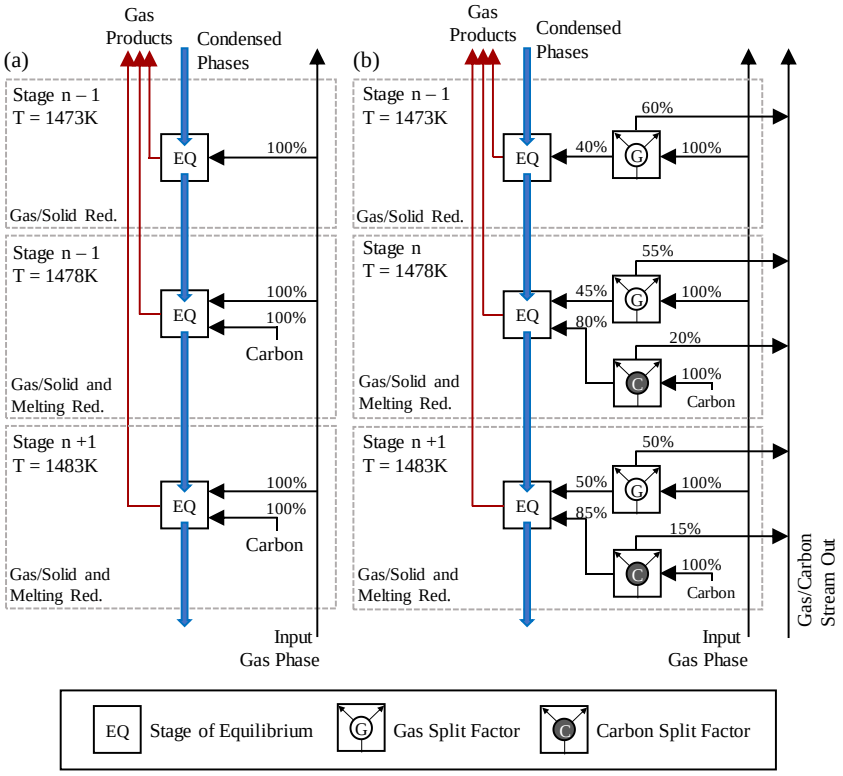

Figura C.4. Modelo termodinâmico de estágios múltiplos (a) sem e (b) com a utilização de *splitters* para considerar restrições cinéticas.

O valor dos *splitters* foi calculado, para cada um dos reatores de equilíbrio utilizados, a partir da razão entre o parâmetro de interesse (nesse caso o grau de redução (RD)) obtido experimentalmente pelo mesmo parâmetro obtido pela simulação, de acordo com a Equação C.1. Assim, sempre que o modelo obter graus de redução (RD) maiores que os experimentais, um valor menor que 1 será obtido a partir da equação. Aplicando esse valor sobre a quantidade de gás redutor ou carbono de entrada em cada reator de equilíbrio, limita-se a quantidade de redutor disponível, consequentemente tratando a cinética de redução de uma forma indireta. O *splitter* é calculado para cada reator de equilíbrio à cada loop de cálculo realizado até que os erros relativos desejados sejam atingidos. Assim, a cada loop de cálculo, o produtório dos *splitters* é ajustado.

$$\text{Splitter (input gas phase and carbon)} = \prod_{Iteration=1}^{n} {RD_{exp}^{T}}\Big/{RD_{sim}^{T}} \quad \text{Equação C.1}$$

Referências

K. Hack: *The SGTE Casebook Thermodynamics at Work*, Woodhead Publishing Limited, Cambridge, England, 2008.